Giant magnetocaloric effect in the (Mn,Fe)NiSi-system

Sagar Ghorai [1,2,*] Rafael Martinho Vieira [3,4,†] Vitalii Shtender [5] Erna K. Delczeg-Czirjak [3,6] Heike C. Herper [3] Torbjörn Björkman [4] Sergei I. Simak [3,7] Olle Eriksson [3,6] Martin Sahlberg [5,8] and Peter Svedlindh [1]

[1]*Department of Materials Science and Engineering, Uppsala University, Box 35, SE-751 03 Uppsala, Sweden*

[2]*Institute of Material Science, Technical University of Darmstadt, 64287 Darmstadt, Germany*

[3]*Department of Physics and Astronomy, Uppsala University, Box 516, SE-751 20 Uppsala, Sweden*

[4]*Physics, Faculty of Science and Engineering, Åbo Akademi University, FI-20500 Turku, Finland*

[5]*Department of Chemistry–Ångström Laboratory, Uppsala University, Box 538, SE-751 21 Uppsala, Sweden*

[6]*WISE - Wallenberg Initiative Materials Science for Sustainability, Department of Physics and Astronomy, Uppsala University, SE-751 20 Uppsala, Sweden*

[7]*Department of Physics, Chemistry and Biology (IFM), Linköping University, SE-581 83 Linköping, Sweden*

[8]*WISE - Wallenberg Initiative Materials Science for Sustainability, Department of Chemistry, Uppsala University, SE-751 20 Uppsala, Sweden*

(Received 11 June 2024; accepted 30 October 2024; published 3 December 2024)

The search for energy-efficient and environmentally friendly cooling technologies is a key driver for the development of magnetic refrigeration based on the magnetocaloric effect (MCE). This phenomenon arises from the interplay between magnetic and lattice degrees of freedom that is strong in certain materials, leading to a change in temperature upon application or removal of a magnetic field. Here we explore in detail an emerging material, $Mn_{1-x}Fe_xNiSi_{0.95}Al_{0.05}$, with an exceptionally large isothermal entropy at room temperature. By combining experimental and theoretical methods we outline the microscopic mechanism behind the large MCE in this material. It is demonstrated that the competition between the Ni_2In-type hexagonal phase and the TiNiSi-type orthorhombic phase, that coexist in this system, combined with the distinctly different magnetic properties of these phases, is a key parameter for the functionality of this material for magnetic cooling.

DOI: 10.1103/PhysRevMaterials.8.124401

I. INTRODUCTION

Materials exhibiting a large magnetic field-induced isothermal entropy change (ΔS_M) are classified as giant magnetocaloric effect (GMCE) materials and are desired for magnetic refrigeration near room temperature [1]. One of the main factors contributing to the GMCE is a magnetostructural transition (MST), where a structural phase transition coincides with a magnetic phase transition, resulting in a large change in the magnetization and magnetic entropy. However, to achieve a GMCE, the system must meet two requirements: a large difference in the magnetic properties of the two structural phases and a narrow temperature range between the magnetic ordering temperature (T_C) and the structural transition temperature (T_{st}). These conditions most likely arise in systems with a strong coupling between the magnetic and lattice degrees of freedom.

The MnTX system (T = Co, Ni and X = Ge, Si) represents a promising class of intermetallic shape-memory compounds that may exhibit an MST [2]. The parent compound, MnNiSi, is known to undergo a structural phase transition from a low-temperature orthorhombic phase (TiNiSi-type, space group *Pnma*) to a high-temperature hexagonal phase (Ni_2In-type, space group $P6_3/mmc$). The orthorhombic phase can be viewed as a distorted version of the hexagonal phase, with the lattice parameters related as $a_{ort} \equiv c_{hex}$, $b_{ort} \equiv a_{hex}$, and $c_{ort} \equiv \sqrt{3}a_{hex}$ [3]. The two phases are illustrated in Fig. 1(a), highlighting similarities and differences between the structures. In the parent compound, the structural, $T_{st} = 1206$ K, and magnetic transition, $T_C = 622$ K, temperatures differ greatly [4,5], indicating that the expected coupled MST is not present. Recently, it has been found that both T_C and T_{st} can be tuned by Mn-site [6], Ni-site [7,8], and Si-site [9–11] chemical substitutions in the MnNiSi parent compound. In the $Mn_{0.5}Fe_{0.5}NiSi_{1-x}Al_x$ compound, an introduction of $1.5 - 2.3\%$ Al shifts both T_C and T_{st} to near room temperature [9] and a MST becomes possible. Owing to the coexistence of the orthorhombic and hexagonal phases for temperatures around the magnetic transition region, the description of T_C for the multiphase mixture (where the two phases coexist) is complex and has not been explored so far. Applying an atomistic spin model in such a complex system raises the challenge of including two sets of exchange parameters, each associated with one phase and with very distinct T_C, which allow for a phase to retain the magnetic order while the other transitions to a paramagnetic state. Moreover, since the relative wt. % of the two structural phases varies with temperature in the magnetic transition region, a concomitant

*Contact author: sagar.ghorai@angstrom.uu.se; sagar.ghorai@tu-darmstadt.de

†Contact author: rafael.vieira@physics.uu.se

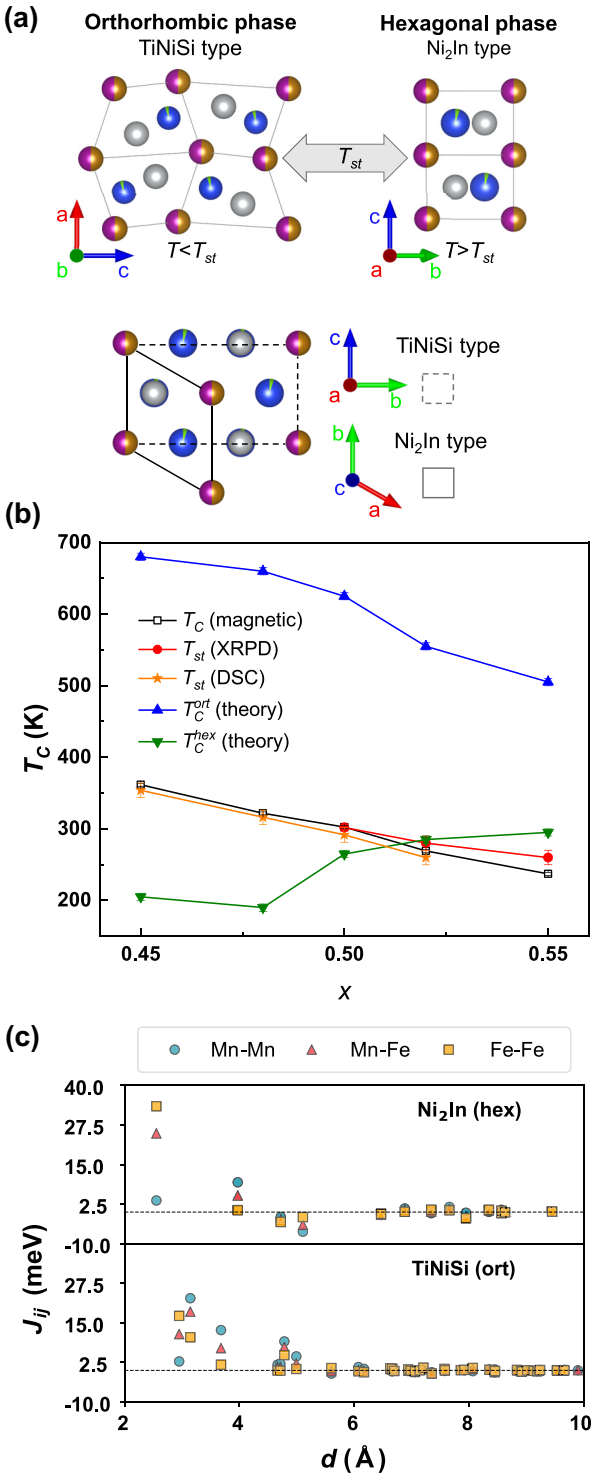

FIG. 1. (a) Hexagonal and orthorhombic phases of $Mn_{0.5}Fe_{0.5}NiSi_{0.95}Al_{0.05}$ obtained from XRPD refinement. The top panel highlights the alterations in the arrangement of the atoms due to the phase transition. The bottom panel illustrates the relation between unit cells. The colors represent the site occupation by the different chemical elements: Mn (pink), Fe (orange), Ni (gray), Si (blue), and Al (green). Plotted with VESTA [12]. (b) Calculated and experimental transition temperatures versus the amount of Fe (x) for the $Mn_{1-x}Fe_xNiSi_{0.95}Al_{0.05}$ system. (c) Calculated exchange parameters J_{ij} for $Mn_{0.5}Fe_{0.5}NiSi_{0.95}Al_{0.05}$ in the hexagonal (top) and the orthorhombic (bottom) phases.

temperature-dependent variation of the exchange parameters (J_{ij}) may be possible, which together with the relative orientation of the magnetic moments will decide T_C of the multiphase mixture, potentially leading also to a significant MCE.

The present work explores in more detail the $Mn_{1-x}Fe_xNiSi_{0.95}Al_{0.05}$ (MnFeNiSiAl) system as a potential GMCE compound near room temperature. Using a combination of first-principles calculations and Monte Carlo simulations, the expected variation of T_C in a multiphase mixture description has been calculated and verified experimentally. A large value of the isothermal entropy change is observed experimentally and explained by the sharpness of the MST. Additionally, by comparing the total energy from the electronic structure calculations, the atomic site occupancy of the Fe/Mn and Ni atoms in the MnFeNiSiAl system has been determined (details in Appendix A).

II. EXPERIMENTAL AND THEORETICAL METHODOLOGY

All compounds studied in this work were synthesized using an arc-melting process. Pieces of the high-purity metals Mn, Fe, Ni, Si, and Al were weighted in certain proportions. During arc melting, oxygen contamination was minimized by flushing the furnace five times with Ar and by melting a Ti getter prior to melting the sample. The samples were turned over and remelted three times to promote homogeneity. Negligible losses of Mn (<1 wt. %) were detected in most cases. In the event of a larger loss, more Mn was added to compensate as only Mn evaporates in these alloys during arc melting. Further, samples were wrapped in Ta foil, placed in a quartz tube, and sealed under vacuum for later annealing at 1073 K for 1 week. Afterwards, samples were quenched in cold water. X-ray powder diffraction (XRPD) data were collected at different temperatures ranging from 265 K to 422 K using a Bruker D8 Advance diffractometer with Cu K_α radiation, with an angle step size of 0.02°. The microstructure was investigated using a Zeiss Merlin scanning electron microscope (SEM) equipped with a secondary electron (SE) detector and an energy-dispersive x-ray spectrometer (EDS). Thermal analysis in the temperature range from 190 K to 650 K was performed using a 204*F*1 Netzsch heat-flux differential scanning calorimeter with aluminium pans. The magnetic properties were investigated in the temperature range from 5 K to 400 K using the Magnetic Property Measurement System (MPMS) and Physical Property Measurement System (PPMS) from Quantum Design.

Magnetic moments and magnetic exchange interactions (J_{ij}) were calculated for the experimental structures and compositions (atomic occupancy and lattice parameters) with the spin-polarized Korringa-Kohn-Rostoker method [13,14] within the atomic sphere approximation (ASA) as implemented in the SPR-KKR code [15]. The chemical disorder was treated within the coherent potential approximation (CPA) [16,17] after verifying that the alloy does not exhibit any tendency to form localized environments (see Appendix B for more details). The one-electron equations were solved within the scalar-relativistic approximation with a minimal basis set (s, p, and d states). The calculations were performed using the Perdew-Wang [18] formulation of the local

TABLE I. Summary of calculated magnetic properties and geometrical parameters from XRPD refinement for different amounts of Fe (x) in the $Mn_{1-x}Fe_xNiSi_{0.95}Al_{0.05}$ system.

	Orthorhombic phase								Hexagonal phase						
x	a (Å)	b (Å)	c (Å)	m_{Mn} (μ_B)	m_{Fe} (μ_B)	m_{Ni} (μ_B)	m_{tot} (μ_B/f.u.)	T_C (K)	a (Å)	c (Å)	m_{Mn} (μ_B)	m_{Fe} (μ_B)	m_{Ni} (μ_B)	m_{tot} (μ_B/f.u.)	T_C (K)
0.45	5.656	3.659	6.929	2.514	1.889	0.158	2.282	680 ± 5	3.978	5.114	2.450	1.901	0.109	2.220	205 ± 5
0.48	5.627	3.667	6.934	2.506	1.873	0.154	2.247	660 ± 5	3.976	5.106	2.436	1.880	0.106	2.180	190 ± 5
0.50	5.598	3.675	6.940	2.462	1.824	0.164	2.201	625 ± 5	3.972	5.106	2.432	1.866	0.104	2.159	265 ± 5
0.52	5.588	3.679	6.907	2.387	1.771	0.211	2.172	555 ± 5	3.970	5.097	2.410	1.841	0.101	2.121	285 ± 5
0.55	5.495	3.771	6.856	2.495	1.872	0.131	2.178	505 ± 5	3.970	5.093	2.408	1.839	0.100	2.101	295 ± 5

spin density approximation for the exchange-correlation functional. For the determination of the J_{ij} parameters the Lichtenstein-Katsnelson-Antropov-Gubanov formalism (LKAG) [19] was considered for the exchange pair interactions. In the LKAG approach the J_{ij} are determined as the energy perturbation, relative to the ground state, induced by an infinitesimal rotation of the local spin moments. The calculations for Mn and Fe were restricted to a cutoff radius of 2.5 (5.0 on the hexagonal cells) lattice units, since more long-ranged interactions are vanishingly small. Including Ni exchange couplings does not significantly alter the mean-field magnetic ordering temperatures for the orthorhombic and hexagonal phases. Including the Ni exchange couplings yields 833 K and 339 K for the mean-field (MFA) magnetic ordering temperatures of the orthorhombic and hexagonal phases, respectively, which can be compared to the corresponding values of 828 K and 338 K excluding the same exchange parameters, justifying our simplification. The magnetic moments and the exchange parameters J_{ij} derived from first-principles calculations were used as input for Monte Carlo (MC) simulations.

The MC simulations were executed with the Uppsala atomistic spin dynamics (UPPASD) code [20,21] using the atomistic Heisenberg Hamiltonian:

$$\mathcal{H} = -\frac{1}{2}\sum_{i \neq j} J_{ij}\mathbf{e_i} \cdot \mathbf{e_j}, \tag{1}$$

which describes the pair exchange interactions between normalized magnetic moment vectors ($\mathbf{e}$). In these simulations, a simulation box of $24 \times 24 \times 24$ unit cells (55 296 spins) with periodic boundary conditions was considered. For each temperature step, we allow for 50 000 MC steps for equilibration followed by 10^5 steps for measurement of the thermodynamic averages. From the average energy [defined by Eq. (1)] for the different temperatures (T), the heat capacity was calculated as $\partial\langle E\rangle/\partial T$ to determine the magnetic ordering temperature. For improved accuracy, a temperature step of 5 K was considered around the peak region. Since the heat capacity peaks at phase transitions, it is a good indicator to find T_C, having the advantage over the magnetization analysis that it allows identifying other order-disorder magnetic phase transitions. This choice was motivated by the results of the Monte Carlo simulations for the hexagonal phase at low temperatures, in which case a noncollinear magnetic configuration is observed.

III. RESULTS AND DISCUSSION

A. First-principles calculations

The unit cell and atom projected magnetic moments have been calculated by *ab initio* theory, both for the orthorhombic and hexagonal phases, and are shown in Table I. A weak dependence between the magnetic moment and the Fe concentration is observed, with the total magnetic moment decreasing with increasing amount of Fe, which is in accordance with experimental results for the orthorhombic phase reported here and in Ref. [22]. Contrary to what is often observed in GMCE materials, the magnetic moments for Mn and Fe sites are similar in the orthorhombic and hexagonal phases. This is in agreement with the results for the MnNiSi and FeNiSi systems in Ref. [23], but in contrast with the results reported for the $Mn_{0.5}Fe_{0.5}NiSi$ system in Ref. [24].

Besides variations in the local magnetic moments, a significant difference in the magnetization between phases can be expected if the phases exhibit a difference in the type of magnetic order or if they have different magnetic ordering temperatures. This is determined by the interatomic exchange parameters of the Heisenberg Hamiltonian [see Eq. (1)], and since *ab initio* theory has the capability to evaluate these parameters [25], it is possible to obtain a parameter-free spin Hamiltonian that, when coupled to Monte Carlo (MC) simulations, gives reliable information of finite temperature magnetism [26].

From a comparison of the calculated exchange parameters, shown in Fig. 1(c), it is observed that, in contrast to the orthorhombic phase, the hexagonal structure possesses non-negligible antiferromagnetic couplings, which explains the low-temperature noncollinear spin structure relaxed for this phase being a consequence of competition between the first (in-plane) and second (between hexagonal planes) nearest neighbors with the third and fourth nearest neighbors (see Appendix C for details). Moreover, it is observed that, for the hexagonal phase, the exchange parameters are much stronger than for the orthorhombic phase. In addition, the long-range nature of the exchange interactions is important for this system; including only exchange parameters within a radius of 6 Å in the Monte Carlo simulations (see below) decreases the magnetic ordering temperature to around 120 ± 20 K. However, some caution is necessary in the analysis of the J_{ij} parameters since the relaxed configurations (noncollinear) in the Monte Carlo simulations do not match the magnetic configuration assumed (collinear ferromagnetic) in the DFT calculations of the J_{ij}. We interpret this disagreement to be a

result of the competition between the antiferromagnetic and ferromagnetic couplings observed in the J_{ij} [see Fig. 1(c)], yielding a noncollinear spin structure due to the higher degree of freedom of the Monte Carlo simulations. In principle, for an ideal Heisenberg magnet, the J_{ij} parameters do not depend on the magnetic configuration considered; however, in practice, this does not always hold true. Experimentally, it is challenging to determine the actual magnetic order of the hexagonal phase for this composition, since the orthorhombic-hexagonal structural transition precedes the estimated magnetic ordering temperature when cooling down the system. In principle, the magnetic properties of the hexagonal phase can be studied by stabilizing the phase at low temperatures with increasing Al doping [27,28]. However, existing magnetic measurements for higher Al concentrations, e.g., in Ref. [28], are not conclusive. Moreover, we note that similar $MnNiSi_xGe_{1-x}$ compounds can display a helimagnetic phase [29].

From Monte Carlo simulations, using the calculated atomic moments and the exchange parameters of Fig. 1(c), an overall decrease of the calculated T_C with increasing amount of Fe is observed for the orthorhombic phase; cf. Fig. 1(b). This trend agrees with the experimental results [see Fig. 1(b)], although the calculated ordering temperature is considerably larger compared to the experimental observations and the decrease of T_C as a function of Fe concentration is smaller than the one measured. Note that the temperature range for the calculated T_C of the orthorhombic phase (see also Table I) is close to the value of the orthorhombic parent compound, MnNiSi (≈600 K). The calculated magnetic transition temperature for the hexagonal phase shows a trend which is opposite to that of the orthorhombic phase, with an increasing amount of Fe. The ordering temperature for this phase is also seen to be much lower compared to the data of the orthorhombic structure, hence displaying a surprisingly strong phase dependence on the ordering temperature.

B. Structural and magnetic phase diagram

To experimentally determine the crystallographic phase contribution, temperature-dependent x-ray powder diffraction (XRPD) measurements have been performed on all compounds that were found to exhibit two major crystallographic phases: the TiNiSi-type orthorhombic phase and the Ni_2In-type hexagonal phase. However, a small amount of $MnZn_2$-type hexagonal impurity phase has also been observed, which is discussed in Appendix D. The relative amount of the two major phases is found to be distinctly temperature dependent. Moreover, the $x = 0.5$ compound is found to undergo a structural phase transition from the low-temperature orthorhombic to the high-temperature hexagonal phase as shown in Fig. 2(a).

Figure 2(b) shows the temperature dependence of the wt. % of the two structural phases, where the crossing of the curves for the different compounds indicates T_{st} for the corresponding compound. T_{st} decreases with increasing amount of Fe. The structural phase change is driven by thermal energy, enabling the distorted orthorhombic structure to transform into the hexagonal structure. A lower value of the c_{hex}/a_{hex} (a_{orth}/b_{orth}) ratio indicates a more stable hexagonal (orthorhombic) structure [30,31]. Figure 2(c) reveals a decreasing trend of the a_{orth}/b_{orth} ratio with increasing amounts of Fe. This trend is much subdued for the c_{hex}/a_{hex} ratio, indicating a more stable orthorhombic structure at lower temperatures [32]. The difference between the c_{hex}/a_{hex} ratio in the hexagonal phase and the a_{orth}/b_{orth} ratio in the orthorhombic phase is proportional to the thermal energy required for the structural phase change. Therefore, the decrease of the difference between c_{hex}/a_{hex} and a_{orth}/b_{orth}, denoted as $\Delta(c/a)$ [$\Delta(c/a) = a_{orth}/b_{orth} - c_{hex}/a_{hex}$], see the orange arrow in Fig. 2(c), with increasing Fe amount indicates a similar decrease of the thermal energy required for the structural phase change to occur. This also explains the decrease of T_{st} with increasing amount of Fe as seen in Fig. 2(c) and Fig. 1(b).

The decrease of the hexagonal lattice parameter ratio c/a with increasing Fe amount leads to a decrease of the interlayer distance for the Mn/Fe atoms separated by a Ni-Si layer along the *ab* plane [cf. Fig. 1(a)]. Since the magnetic properties of the MnNiSi system are highly sensitive to the Mn-Mn distance [33], the structural phase change will influence the magnetic exchange parameters of the system. In Fig. 2(e), the temperature-dependent magnetization for the studied compounds is shown. The temperature hysteresis of the magnetic transition, while decreasing and increasing the temperature, indicates a first-order nature of the phase transition. Also, T_C decreases with increasing amount of Fe, similar to the trend of T_{st}. Below we discuss how the structural transition influences the magnetic transition at T_C.

Significantly, as revealed in Fig. 2(b) a non-negligible fraction (≈20%) of the hexagonal phase remains at low temperature in all of the studied compounds. A similar observation was reported in Ref. [27] for the $Mn_{0.5}Fe_{0.5}NiSi_{1-x}Al_x$ system, where the two phases were shown to coexist at room temperature for Al concentrations between 0.045 and 0.055. Below and above this concentration interval, the orthorhombic and hexagonal phases dominated, respectively, highlighting the role of Al for the stability of the hexagonal phase. Interestingly, it was observed in the same work that T_C decreases with an increasing amount of Al [27]. Since neither Al nor Si contributes directly to the magnetic properties and since the low level of doping considered did not induce any significant change in the lattice parameters, it is reasonable to assume that the magnetic properties of the pure orthorhombic and hexagonal phases did not change to any significant extent. This hints that the interaction between the two phases plays a significant role in the magnetic properties of the composite compound.

In addition to XRPD, the results from temperature-dependent differential scanning calorimetry (DSC) of the studied compounds are shown in Fig. 2(d). As there is no magnetic field applied during the DSC measurements, the peaks observed in Fig. 2(d) are mostly indicative of structural phase transitions. As seen in Fig. 2(e), the temperature hysteresis of the structural transition yields a corresponding temperature hysteresis of the magnetic transition. Moreover, as the structural phase transition temperature T_{st} of the compounds occurs in close vicinity of T_C [cf. Fig. 2(b)], a coupled MST can be expected in the MnFeNiSiAl compounds. The strength of the MST mostly depends on how close T_C and T_{st} are, along with how sharp the transitions are with respect to temperature. As seen in Fig. 2(b), the sharpest structural transition is observed for the $x = 0.5$ compound, which along

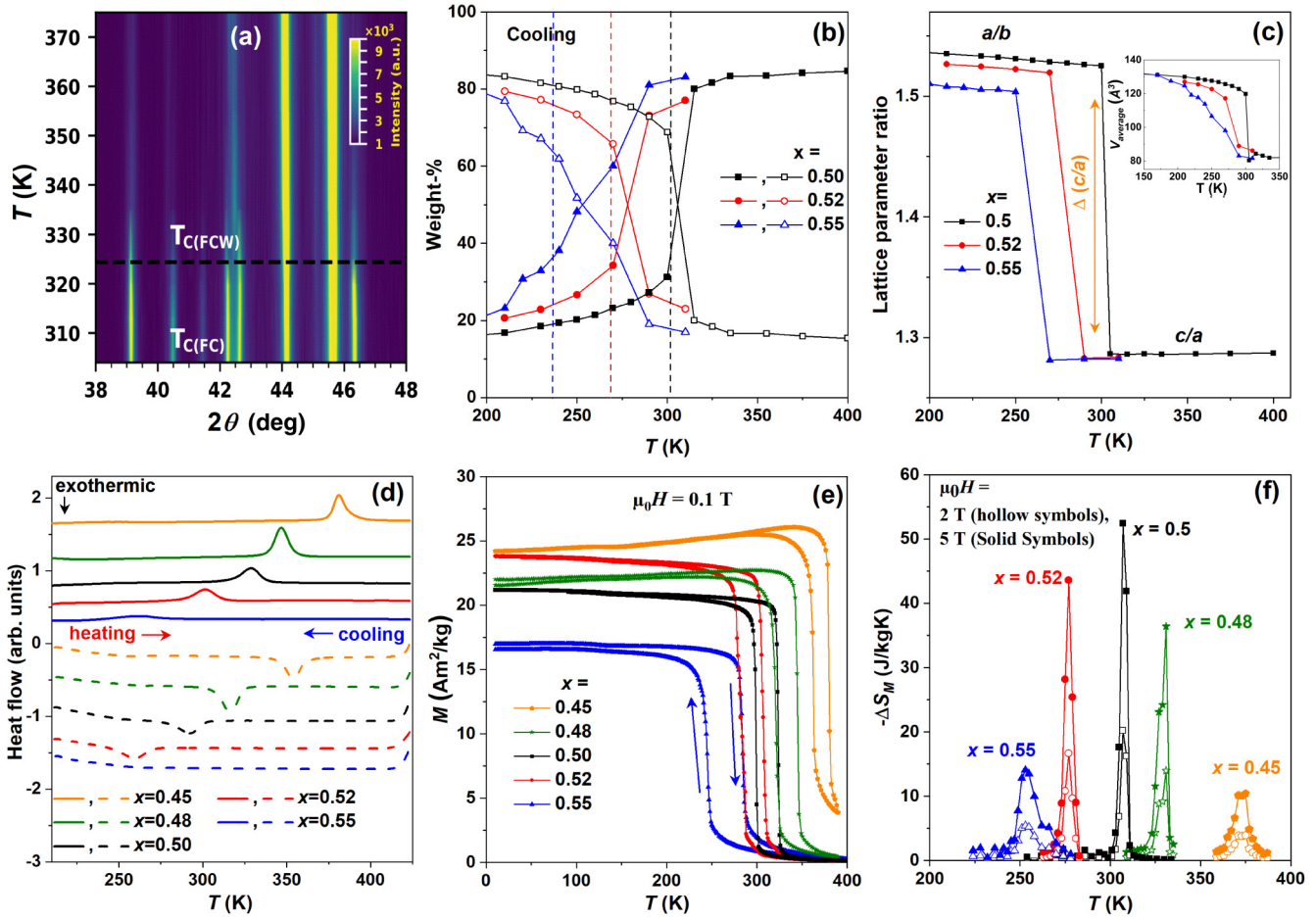

FIG. 2. (a) Temperature-dependent x-ray powder diffraction pattern of $Mn_{0.5}Fe_{0.5}NiSi_{0.95}Al_{0.05}$. The dashed horizontal line indicates T_C during heating ($T_{C(\mathrm{FCW})}$); T_C during cooling (FC) is at 300 K. (b) Temperature-dependent wt. % of the two structural phases for the $x = 0.5, 0.52$, and 0.55 compounds calculated from the XRPD data recorded during the cooling cycle. The hollow and solid symbols represent the orthorhombic and hexagonal phases, respectively. The dashed color-coded vertical lines represent T_C of the corresponding compounds. (c) Temperature-dependent variation of the hexagonal lattice parameter ratio c/a and the equivalent lattice parameter ratio of the orthorhombic phase a/b. The inset shows the temperature dependence of the average volume of the unit cell for the different compounds. The error in the phase wt. % is less than 0.5% and the error in the lattice parameter data is in the order of 10^{-3} Å and therefore not included in the figure. (d) Differential scanning calorimetry versus temperature for the studied compounds during cooling and heating cycles. (e) Temperature-dependent magnetization and (f) temperature-dependent isothermal entropy change for the different compounds.

with the smallest separation between T_C and T_{st} strongly suggests that this compound exhibits the strongest MST. The $x = 0.55$ compound in comparison exhibits a broad structural transition, which together with more separated values for T_C and T_{st} imply a weaker MST. Therefore, it is expected that the $x = 0.5$ compound will exhibit the largest GMCE among the studied compounds.

C. GMCE

The magnetocaloric effect can be described as a system-dependent spin-lattice interaction phenomenon. Under adiabatic conditions, the sum of the magnetic and lattice entropies of a system is conserved (here neglecting the electronic entropy contribution). Therefore, a change in magnetic entropy with the application or removal of a magnetic field will induce a change in the lattice entropy and hence the temperature of the material. This change in temperature is related to the change of the isothermal entropy (ΔS_M) of the system, which is an important characteristic of the magnetocaloric effect. The magnetic field induced ΔS_M can be derived from the Maxwell relation [41]

$$\Delta S_M(T, H_f) = -\mu_0 \int_0^{H_f} \left(\frac{\partial M}{\partial T}\right)_H dH. \tag{2}$$

From Eq. (2), it is clear that a high value of ΔS_M requires a large change of the temperature and magnetic field-dependent magnetization. As described in the previous section, the strongest MST is expected for the $x = 0.5$ compound and the largest value of ΔS_M is also observed for this compound [cf. Fig. 2(f)]. The MST is also associated with a change in lattice volume. The inset of Fig. 2(c) shows the change in average lattice volume (scaled with the wt. % for each phase) for the different compounds. Noticeably, the lower and upper limits of the lattice volume for the compounds are almost the same owing to the small difference in chemical composition between the compounds. However, the volume change is sharper

TABLE II. Magnetocaloric properties of the here studied compounds (*) compared with data reported for other GMCE materials near room temperature, at an external magnetic field of $\mu_0 H = 2$ T. Values with ' symbols have been calculated by digitizing the data from the literature. For definition of RCP and RC, see main text.

Sample	T_C^{FC} (K)	$-\Delta S_M$ (J/kg K)	RCP (J/kg)	RC (J/kg)	Ref.
$Mn_{0.55}Fe_{0.45}NiSi_{0.95}Al_{0.05}$	362	3.93	36.9	30.8	*
$Mn_{0.52}Fe_{0.48}NiSi_{0.95}Al_{0.05}$	322	14.0	82.9	59.6	*
$Mn_{0.50}Fe_{0.50}NiSi_{0.95}Al_{0.05}$	304	20.2	86.9	71.6	*
$Mn_{0.48}Fe_{0.52}NiSi_{0.95}Al_{0.05}$	269	16.7	85.2	67.3	*
$Mn_{0.45}Fe_{0.55}NiSi_{0.95}Al_{0.05}$	237	5.4	64.5	51.99	*
$Mn_{0.50}Fe_{0.50}NiSi_{0.95}Al_{0.05}$	∼316	∼16	∼70		[9]
$Mn_{0.5}Fe_{0.5}NiSi_{0.94}Al_{0.06}B_{0.005}$	∼280	22	66	64	[24]
$Mn_{0.6}Fe_{0.4}NiSi_{0.93}Al_{0.07}$	∼245	9.3			[28]
$Fe_{0.95}V_{0.05}MnP_{0.5}Si_{0.5}$	318	9.1	103	57.2'	[34]
$FeMn_{0.95}V_{0.05}P_{0.5}Si_{0.5}$	322	13.1	130	120.8'	[34]
Gd	295	6.1	240		[35]
$La(Fe_{0.98}Mn_{0.02})_{11.7}Si_{1.3}H$	312	13			[36]
$Fe_{80}Pt_{20}$	290	∼10			[37]
$Mn_{1.2}Fe_{0.8}P_{0.75}Ge_{0.25}$	288	20			[38]
$MnFeP_{0.52}Si_{0.48}$	268	10			[39]
$La_{0.5}Pr_{0.2}Ca_{0.1}Sr_{0.2}MnO_3$	296	1.8	147	112.6'	[40]

for the $x = 0.5$ compound compared to the other compounds. All these facts indicate that the strongest MST is found for the $x = 0.5$ compound. As a result, the highest value of ΔS_M is observed [cf. Fig. 2(f)] for the $x = 0.5$ compound, followed by the $x = 0.52$ and $x = 0.55$ compounds in ascending order. A similar trend of ΔS_M is observed for compounds where the Fe content is lower than $x = 0.5$, i.e., this trend is also observed for the $x = 0.48$ and $x = 0.45$ compounds. This suggests that below and above the value of $x = 0.5$, the structural transition becomes less and less sharp, leading to lower values of ΔS_M.

The relative cooling power (RCP) and the refrigerant capacity (RC) can be used to quantify the temperature range over which the GMCE is useful for magnetic refrigeration. The relative cooling power is defined as [42]

$$\mathrm{RCP} = -\Delta S_M^{\max} \times \Delta T_{\mathrm{FWHM}}, \tag{3}$$

where $-\Delta S_M^{\max}$ is the maximum value of the isothermal entropy change and ΔT_{FWHM} is the corresponding full width at half maximum. The refrigerant capacity is instead defined as [43]

$$\mathrm{RC} = \int_{T_1}^{T_2} -\Delta S_M(T)dT, \tag{4}$$

where T_1 and T_2 correspond to the temperatures where the value of $-\Delta S_M$ is half of $-\Delta S_M^{\max}$. The values of RCP and RC are given in Table II for the compounds studied here. The experimental data of the FeMnNiSiAl system is in Table II compared to data reported for other GMCE materials. To the best of our knowledge, compared to other GMCE compounds, the $x = 0.5$ compound exhibits one of the largest values of ΔS_M ever reported. In addition, the relative cooling power and the refrigerant capacity are competitive to that of other systems listed in Table II.

In addition to Maxwell's relation, the Clausius-Clapeyron (CC) relation can also be used to calculate the isothermal entropy change [44,45]. A detailed calculation of $-\Delta S_M$ using the CC relation as well as a comparison with $-\Delta S_M$ calculated using Maxwell's relation for the $x = 0.5$ compound is presented in Appendix E. Although there is a good agreement between these two methods, Maxwell's relation has been adopted in this work, as the CC relation assumes a 100% magnetic phase change at T_C without accounting for the lattice volume change in the studied (Mn,Fe)NiSi system.

D. Coupled phase transition

In the MnNiSi system, the magnetic properties are highly sensitive to the distances between the magnetic atoms [33]. A detailed analysis of Fe/Mn distances for the studied compounds is included in Appendix F. However, owing to the presence of two phases, the orthorhombic and hexagonal structures near the magnetic phase transition temperature, it is not straightforward to establish a clear relationship between the magnetic properties and the Fe/Mn distances. The magnetic and structural transitions are coupled in the MnFeNiSiAl compounds and the coexistence of the two phases in the experimental samples is important to take into account for realistic simulations of the magnetic properties. A model describing this situation has been proposed by Skomski and Sellmyer [46], where the magnetic ordering temperature was calculated for a nanocomposite material consisting of two coexisting magnetic phases, one with low and one with high magnetic transition temperature. The calculations of Ref. [46] showed that there would only be one magnetic transition temperature, even for a multiphase mixture with distinctly different Heisenberg interactions. As discussed in this work, the T_C of the multiphase mixture, in general, was found to be larger than the volume average of the transition temperatures for the involved phases.

1. Magnetic mixture setup

The situation for the MST of MnFeNiSiAl is more complex than the model described in Ref. [46], since the weight percent of the involved phases is strongly temperature dependent in the transition region [cf. Fig. 2(b)] and the phases involved have different structures with the Mn/Fe sites, which define the magnetic sublattice, having different numbers of neighbors. With the interest of exploring the effects of phase coexistence for varying concentrations, we explore a simplified model where the phases form a homogeneous mixture as in an idealized disordered alloy. With this goal in mind, we start to set up a representation that can describe the coexistent phases on the same basis and proceed to a mapping of the magnetic properties of the hexagonal and orthorhombic phases into this basis.

As illustrated in Fig. 6, both hexagonal and orthorhombic phases can be represented on a TiNiSi-type structure, making an ideal starting point. Within this representation, the atom's positions in the orthorhombic phase differ from the hexagonal phase by displacements, $\mathbf{d_i}$, from high-symmetry Wyckoff positions [see Fig. 6(a)]. Knowing $\mathbf{d_i}$, every site in the orthorhombic phase can be mapped to its analogous site in the hexagonal phase (TiNiSi representation). This allows us not only to map properties as the local magnetic moments

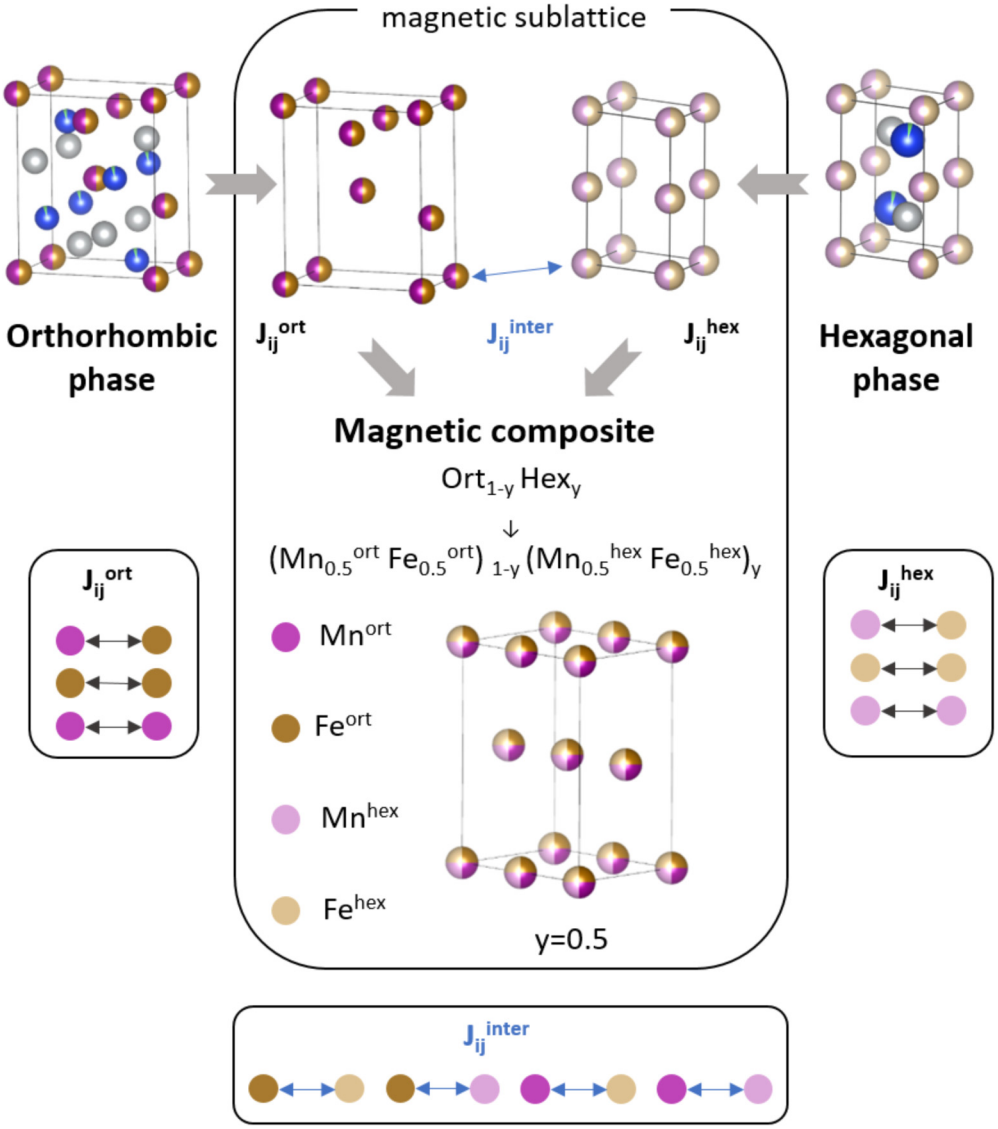

FIG. 3. Scheme of the setup used to describe the magnetic multiphase mixture in the Monte Carlo simulation. Effectively, the magnetic multiphase mixture is described as an alloy with four magnetic species: Mn^{ort} and Fe^{ort} with the magnetic properties of the orthorhombic phase and Mn^{hex} Fe^{hex} with the magnetic properties of the hexagonal phase. More details in text.

but also to map the J_{ij} parameters of the phases despite their distinct coordination.

One can associate an interaction vector, $\mathbf{u}_{ij}$, to each pair of interacting spins in the Heisenberg Hamiltonian [see Eq. (1)], with $\mathbf{u}_{ij}$ connecting the sites i and j coupled by the respective J_{ij} exchange parameter. Analogous to the mapping between sites of the orthorhombic and hexagonal phases with $\mathbf{d_i}$, the interaction vectors of both phases can be related by $\mathbf{u}_{ij}^{ort} = \mathbf{u}_{ij}^{hex} + \mathbf{d_i} + \mathbf{d_j}$. Then, matching the interaction vectors allows us to map the exchange parameters of the hexagonal phase, J_{ij}^{hex}, with the ones of the orthorhombic phase, J_{ij}^{ort}, despite the different coordination number of Mn/Fe sites between the structures. Note that the atomistic Heisenberg Hamiltonian [Eq. (1)] does not depend explicitly on the site positions. Given that the local spin moments and J_{ij} parameters can be mapped one to one, the orthorhombic and hexagonal phases can be simulated in the same setup.

Having established that we can describe both phases within the same structure, we continue by describing the mixture of both phases as an ideal disordered alloy $(Mn^{ort}Fe^{ort})_{(1-y)}(Mn^{hex}Fe^{hex})_y$, with y being the weight of the hexagonal phase (see Fig. 3). The Mn^{hex} and Fe^{hex} sites have the magnetic properties of their respective species in the hexagonal phase, including identical local magnetic moments, and interaction with each other using the exchange parameters of the hexagonal phase, J_{ij}^{hex}. The Mn^{ort} and Fe^{ort} sites have analogously the magnetic properties of the orthorhombic structure. By considering the mixture as an ideal disordered, we do not assume the formation of any specific microstructure, with every site of the simulation box populated randomly so that the fractions of Mn^{hex}, Fe^{hex}, Mn^{ort}, and Fe^{ort} defined by y are respected. In the trivial case of $y = 0.5$, this means that by, picking a random site in the simulation box, we have an equal probability of finding either species. For other

values of y there will be a different proportion between hexagonal (each with a $y/2$ fraction) and orthorhombic species $[(1-y)/2]$; for example, in the case of $y = 0.33$ (33% of hexagonal weight), the simulation box with a total of 55 296 sites contains 9216 Mn^{hex} atoms, 9216 Fe^{hex} atoms, 18 432 Mn^{ort} atoms, and 18 432 Fe^{ort} atoms, randomly distributed among the sites.

Note that this coexistence of magnetic phases in the simulations box introduces the need to account for the interphase magnetic interaction, i.e., the interactions between the orthorhombic and hexagonal species, J_{ij}^{inter} (e.g., Fe^{hex}-Mn^{ort} couplings; see Fig. 3), which are unknown to us. However, the calculation of J_{ij}^{inter} is far from trivial, as it requires the modulation at DFT level of the interface between phases; instead we make an educated guess of these parameters. Since it is reasonable to assume that the real J_{ij}^{inter} parameters should have a behavior somewhere in between J_{ij}^{ort} and J_{ij}^{hex}, we perform for every y composition a set of calculations with $J_{ij}^{inter} = J_{ij}^{ort}$ meaning that the exchange parameter of, e.g., Fe^{hex}-Mn^{ort} coupling is equal to its analog Fe^{ort}-Mn^{ort} and another set of calculations with $J_{ij}^{inter} = J_{ij}^{hex}$. The main idea behind this approach is to define as a first approximation a window (see Fig. 4 and Fig. 12 in Appendix G) for the magnetic properties, which should include the proper properties of the magnetic mixture.

2. Model results

Figure 4 shows the computed magnetic ordering temperature for the magnetic multiphase mixture as a function of the weight percent of the hexagonal phase, y. It can be seen that the window for a room temperature T_C ranges from 40% concentration of hexagonal phase to a concentration of 75%. In addition to the Curie temperature also the average magnetization [cf. Fig. 5(a), with details given in Appendix G) and the magnetic structure are affected by the mixture of orthorhombic and hexagonal phases, as can be seen in the upper and bottom panels of Fig. 4. Using J_{ij}^{ort} for the interface exchange constants conserves ferromagnetic ordering at low fractions of the hexagonal phase yielding a magnetic ordering temperature almost independent of the fraction of the hexagonal phase [cf. Fig. 5(a)]. Assuming instead that the interface exchange interactions are dominated by J_{ij}^{hex} leads to a fast drop of the ferromagnetic ordering temperature with an increasing amount of the hexagonal phase. In a realistic scenario, the exchange interactions will be a mixture of both extremes such that with an increasing fraction of the hexagonal phase the competition between the AFM couplings from the hexagonal phase and the FM couplings from both phases will also increase, which in order to be accommodated favor an increasingly noncollinear arrangement of the magnetic moments.

These results show that the coexistence of phases can have a considerable impact on the magnetic properties and suggest that the structural component is driving the MST, since the growth of the hexagonal phase in the magnetic multiphase mixture drives T_C to the experimental range of magnetic transition temperatures. In order to explore this idea, our model has been expanded to include the variation of the hexagonal phase with temperature. From the calculated

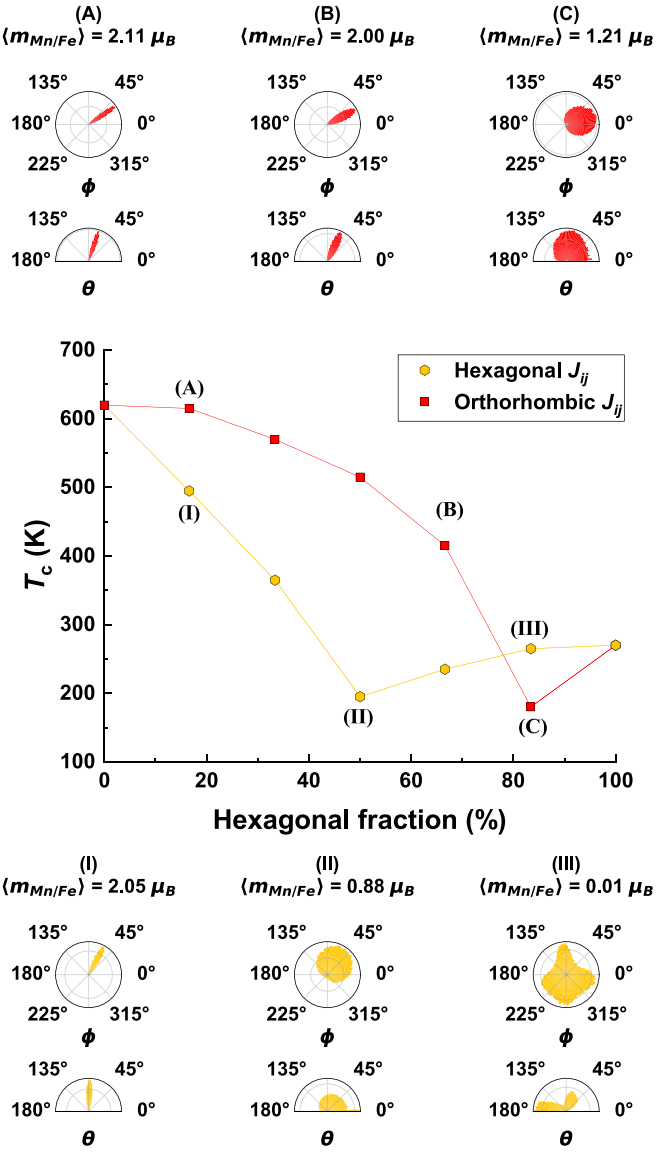

FIG. 4. Calculated magnetic transition temperature from Monte Carlo simulations plotted against the amount of hexagonal phase in the multiphase mixture. As the interface exchange parameters J_{ij}^{inter} between the hexagonal and orthorhombic phases are unknown, two extreme cases are considered. In the middle panel, the orange squares represent when $J_{ij}^{inter} = J_{ij}^{ort}$ and the yellow hexagons represent when $J_{ij}^{inter} = J_{ij}^{hex}$. These cases establish a temperature range where the true value of T_C should be. In the upper (bottom) panel, A, B, and C (I, II, III) depict the statistical spin distribution in spherical coordinates (azimuthal angle ϕ, in the x-y plane, and polar angle θ) of the thermalized magnetic spin configuration at 25 K for the interface J_{ij}^{inter} set of the orthorhombic (hexagonal) phase. The respective average magnetization per magnetic site is also shown.

temperature-dependent magnetization curves, a magnetization surface $M(T, y)$, being a function of temperature (T) and the hexagonal phase fraction in the multiphase mixture (y), has been constructed [cf. Fig. 5(a)]. Combining this data with the hexagonal phase wt. % derived from the XRPD results [cf. Fig. 2(b)] allowed us to calculate the expected temperature dependence of the magnetization taking into account

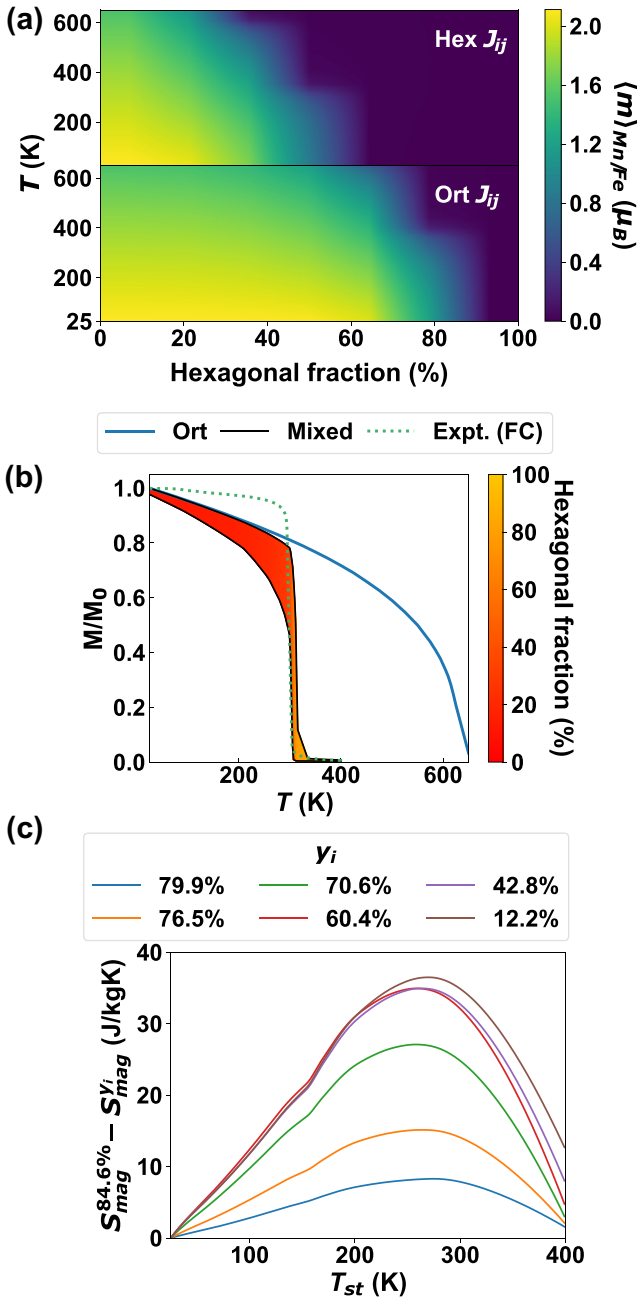

FIG. 5. (a) Calculated average magnetization as a function of temperature and the hexagonal phase wt. % for the $Mn_{0.5}Fe_{0.5}NiSi_{0.95}Al_{0.05}$ compound. (b) Calculated (solid lines) and measured (green dotted line) temperature-dependent normalized magnetization. The results from MC simulations for the pure orthorhombic phase and the multiphase mixture are plotted in blue and black solid lines, respectively. The upper and lower curves of the mixed phase refer to the two extreme cases for the unknown J_{ij}^{inter} and define the region where the true result for the multiphase mixture is expected. The region has been colored according to the temperature-dependent hexagonal wt. % derived from the XRPD results (excluding the impurity phase). (c) Calculated change of magnetic entropy associated with a magnetic field-induced increase of the hexagonal phase fraction from y_i to y_f at the structural transition temperature T_{st}. The different curves correspond to different initial hexagonal weights y_i. The value 84.6% corresponds to the maximum value of y for the $x = 0.5$ compound at $T > T_{\text{st}}$.

the temperature dependence of the hexagonal phase. The results are displayed in Fig. 5(b) in which the experimental data has been included for comparison as well as the magnetization curve simulated for the pure orthorhombic phase.

The proposed model provides a good description of the experimental results, supporting the picture of an MST with the loss of magnetization and magnetic order induced by the structural change. Moreover, a T_C of 455 K has previously been reported for the $Mn_{0.5}Fe_{0.5}NiSi$ compound [9], considerably higher than the one measured here for $Mn_{0.5}Fe_{0.5}NiSi_{0.95}Al_{0.05}$ (≈300 K). Such small doping with Al should not alter the magnetic properties of the pure hexagonal and orthorhombic phases. Instead, the difference in T_C values can be linked to the lower concentration of the hexagonal phase observed at low temperature in Ref. [9], supporting the hypothesis that it is the mixture of hexagonal and orthorhombic phases which determines the MST and in particular the magnetic transition temperature of the multiphase mixture.

Another argument for the structural transition leading to the MST can be found from the rate of decrease of the magnetic ordering temperature with increasing concentration of Fe. A comparison between the theoretically calculated T_C values for the pure phases and the experimental values in Fig. 1(b) reveals that theory predicts a more modest decrease rate than the one measured. Note that the calculations only consider the magnetic subsystem, i.e., the calculations do not consider the weights of the hexagonal and orthorhombic phases and how these are affected by the Fe concentration. The phase weights for the $x = 0.50 - 0.55$ compounds are shown in Fig. 2(b). At constant temperature below the structural transition temperature T_{st}, the phase weight for the hexagonal phase increases with increasing x. Therefore, it is clear that the concentration of Fe helps to stabilize the hexagonal phase.

The heat capacity of the spin system (C_{mag}) was calculated to estimate the magnetic entropy contribution to the GMCE. The calculations were performed for zero magnetic field and a magnetic field of $H = 2$ T, with $J_{ij}^{\text{inter}} = J_{ij}^{\text{ort}}$ (cf. Appendix G for details). The results reveal that close to room temperature the temperature dependence of the magnetic energy is dominated by the temperature dependence of the hexagonal phase suppressing the effect of the magnetic field. Thus calculations using the measured temperature-dependent weights for the hexagonal phase [$y(T)$] of the $x = 0.5$ compound, as used for the calculation of the magnetization in Fig. 5(b), would underestimate the change of magnetic entropy since $y(T)$ under a magnetic field is unknown. Instead, the change of magnetic entropy is calculated as

$$S_{\text{mag}}^{y_f}(T_{\text{st}}) - S_{\text{mag}}^{y_i}(T_{\text{st}}) = \int_0^{T_{\text{st}}} \frac{C_{\text{mag}}(T, y_f) - C_{\text{mag}}(T, y_i)}{T} dT. \tag{5}$$

In this expression, we assume a sharp first-order structural transition and take into account that $\Delta S_{\text{mag}} = S_{\text{mag}}^{y_f} - S_{\text{mag}}^{y_i}$ for a magnetic multiphase mixture will depend on the initial (y_i) and final (y_f) values of the hexagonal phase concentration. While the magnetic field dependence is not explicit in Eq. (5), the difference between y_i and y_f can be interpreted as the

change of the hexagonal phase weight induced by a magnetic field.

From Fig. 2(b) it is clear that, at high temperature ($>T_{st}$), the maximum value of y is $\approx$84.6% for the $x = 0.5$ compound, which we take as y_f in the calculations. However, the value of ΔS_{mag} will be different if y_f is reached from different initial values of y_i near the beginning of the structural phase transition, as shown in Fig. 5(c). It can be noted that the magnitude of the calculated ΔS_{mag} is larger than the measured value of 20 J/(kg K) for $y_i \leqslant 70\%$, but the correct order of magnitude of this calculation highlights the importance of the magnetic field induced change of the hexagonal phase concentration to explain the measured values of the isothermal entropy change. Besides, the lattice contribution to the entropy variation often counteracts the magnetic contribution, reducing the total value of the entropy change. The calculated ΔS_{mag} also highlights that a relatively small field-induced change of the hexagonal concentration is enough to achieve a significant entropy change. Moreover, the peak value of ΔS_{mag} close to the measured transition temperature suggests that the magnetic entropy also plays a role in triggering the structural transition. Further verification of this coupling requires the computation of the free energies. However, the computation of the vibrational entropy constitutes a problem as the Debye's model is not reliable in these compounds, also observed for FeNiSi in Ref. [23], and the hexagonal phase is dynamically unstable at 0 K, not allowing a standard treatment within the harmonic approximation.

IV. CONCLUSIONS

In conclusion, we have shown that it is the mixture and coexistence of the hexagonal and orthorhombic phases (that have a dichotomy in the nature of the interatomic exchange) in the $Mn_{1-x}Fe_xNiSi_{0.95}Al_{0.05}$ system that determines the properties of the MST. Considering the experimentally determined temperature dependence of the two phases close to the structural transition T_{st} and using the interatomic exchange parameters for the two phases calculated by *ab initio* theory as input in atomistic Monte Carlo simulations, it is shown that the magnetic ordering temperature T_C of the multiphase mixture material can be quantitatively predicted. Experimental results reveal that the strength of the MST of the $Mn_{1-x}Fe_xNiSi_{0.95}Al_{0.05}$ system, and its relevance for the GMCE, is governed by the sharpness of the structural transition with respect to temperature. Moreover, theoretical calculations of the magnetic entropy contribution to the GMCE highlight the importance of a magnetic field-induced change of the phase concentrations at the MST to explain the measured isothermal entropy change. This finding calls for in-field experimental studies of the structure close to the MST. Overall we argue that the approach used here combining *ab initio* theory with experimental studies with a focus on the mixture and coexistence of structural phases close to a MST provides a new avenue to find materials with improved GMCE and forms a pathway for further investigations.

All data that support the findings of this study are included within the article.

ACKNOWLEDGMENTS

The authors thank the Swedish Foundation for Strategic Research (SSF), project "Magnetic materials for green energy technology" (Contract No. EM-16-0039) for financial support. The authors acknowledge support from STandUPP and eSSENCE. R.M.V and T.B. acknowledge support from the Magnus Ehrnrooth Foundation. R.M.V. thanks Nuno Fortunato for the discussion related to the Debye model calculations. E.D., O.E., and M.S. acknowledge support from the Wallenberg Initiative Materials Science for Sustainability (WISE) funded by the Knut and Alice Wallenberg Foundation (KAW). O.E. acknowledges support from the Swedish Research Council (VR) and the ERC (FASTCORR project). M.S. Acknowledges support from the Swedish Research Council (grant 2022-03069). S.I.S. acknowledge the support from the Swedish Research Council (VR) (Grant No. 2023-05247), and the Swedish Government Strategic Research Areas in Materials Science on Functional Materials at Linköping University (Faculty Grant SFO-Mat-LiU No. 2009-00971). The computations were enabled by resources provided by the National Academic Infrastructure for Supercomputing in Sweden (NAISS), partially funded by the Swedish Research Council through Grant Agreements No. 2022-06725 and No. 2018-05973, and by the CSCIT Center for Science, Finland. O.E and E.D. acknowledge support from the Wallenberg Initiative Materials Science for Sustainability (WISE) funded by the Knut and Alice Wallenberg Foundation (KAW).

S.G. and R.M.V. contributed equally to this work. S.G. and R.M.V. took the leading role in the experimental and theoretical analysis of this work, respectively, as well as prepared the first draft of the manuscript. V.S. prepared the compounds and performed the structural analysis. M.S. and P.S. supervised the experimental parts of this work. S.I.S. constructed the special quasirandom, ordered, and phase-separated supercell structures. O.E. proposed to explore the phase mixing of the multiphase mixture material. E.K.D.-C. and R.M.V. performed the first-principles calculations and data analysis. T.B. and H.C.H. provided technical support for the DFT calculations. H.C.H., O.E., and T.B. supervised the theoretical parts of this work. All authors discussed the results and contributed to the writing of the manuscript.

The authors declare no competing interests.

APPENDIX A: ATOMIC SITE OCCUPANCY

It is difficult to distinguish between Mn/Fe and Ni when determining which Wyckoff positions these species occupy using XRPD. From the literature, it is ambiguous if Ni occupies the 2*a* site or the 2*d* site in the high symmetry hexagonal phase or if there is a random distribution of Mn/Fe/Ni between the 2*a* and 2*d* sites [47]. To clarify this ambiguity, we compared the total electronic energy of the two possible arrangements, considering also intermediate site distributions with Ni mixing with Mn/Fe for the $Mn_{0.5}Fe_{0.5}NiSi_{0.95}Al_{0.05}$ composition. The total energies were calculated using the exact muffin-tin orbital (EMTO) method [48–50] for the different occupations with the soft-core approximation. As the calculations in the main text, the chemical disorder was treated

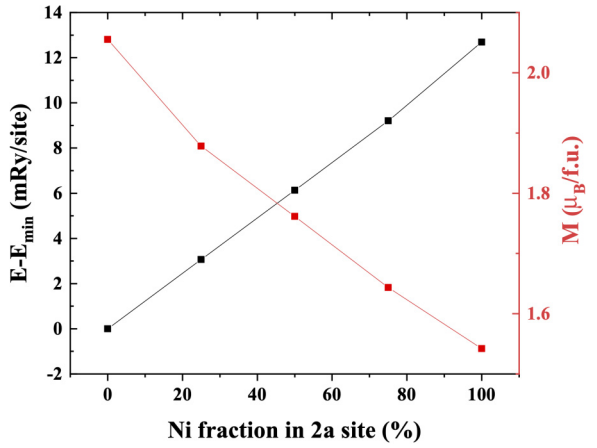

FIG. 6. Calculated total electronic energy (black squares) and magnetic moment (red squares) versus Ni occupation of 2*a* Wyckoff positions in the hexagonal phase. Energies are displayed relative to the minimum energy.

within CPA [16,51] and the scalar-relativistic approximation using the Perdew-Wang [18] exchange-correlation functional. The electrostatic correction to the single-site CPA was considered via the screened impurity model [52] with a screening parameter of 0.6. The Green's function was calculated for 16 complex energy points distributed exponentially on a semicircular contour including states within 1.1 Ry below the Fermi level. For the one-center expansion of the full charge density, a $l^h_{\max} = 8$ cutoff was used.

The results in Fig. 6 show that it is energetically favorable for Ni to occupy the 2*d* Wyckoff position, in agreement with Ref. [23], and that it is reasonable to assume a small degree of mixing (<20%) between Ni and Mn/Fe sites for the annealing temperature used in the sample preparation. The calculations also predict that such an arrangement will maximize the total magnetic moment (see Fig. 6), mainly by the increase of the atomic magnetic moment of Ni (not shown). The high sensitivity on the Wyckoff positions and lattice parameters raises the question if one needs to consider thermal effects on the lattice parameters for an accurate Curie temperature calculation. Still, the measured data [see Fig. 2(c)] reveal that the lattice parameter ratios of each phase do not vary significantly in the temperature range of the phase transition.

APPENDIX B: Ni-Si BONDS

In Ref. [31], the structures of FeNiSi and MnNiSi in the orthorhombic phase were analyzed from neutron diffraction results and the alteration of the Ni-Si framework geometry if the interstitial space was populated either by Fe or Mn was discussed in detail by the authors. This different arrangement raises the question if in the $Mn_{0.5}Fe_{0.5}NiSi$ structure the Ni-Si framework is arranged in an intermediate geometry or if it is dependent on the local environment. If the latter case is true, the description of the magnetic properties becomes more complex with the likelihood of local mechanisms. Since the analysis of the XRPD patterns cannot distinguish between these two cases, we performed structural relaxations in VASP [53–55] (PAW method) for $2 \times 2 \times 2$ supercells with three different patterns of Mn-Fe occupation in

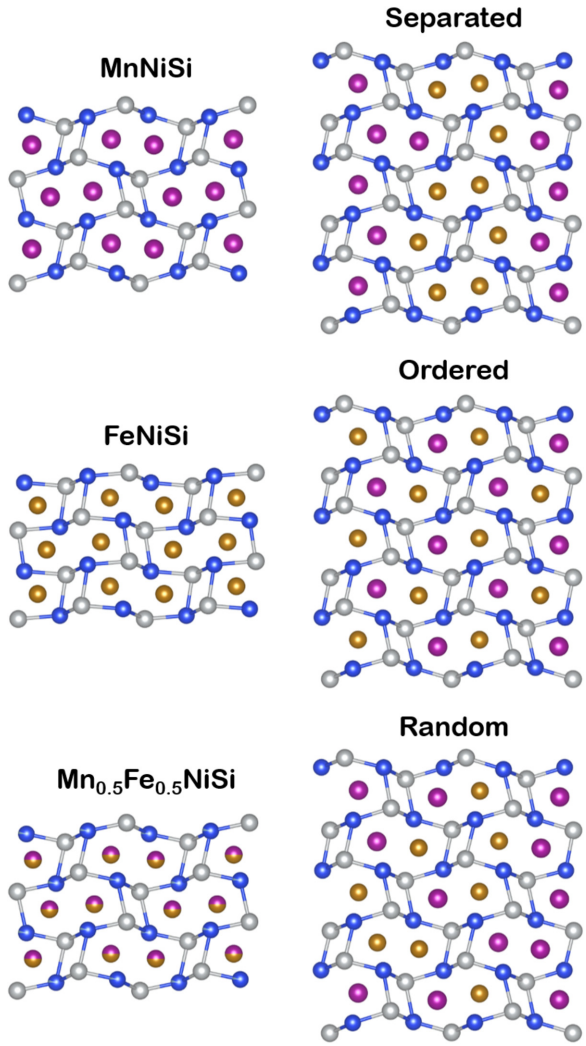

FIG. 7. Ni-Si chains have different geometries in the MnNiSi and FeNiSi compounds. In the XRPD refined structure for the $Mn_{0.5}Fe_{0.5}NiSi_{0.95}Al_{0.05}$ compound, the Ni-Si bonds are arranged as an intermediate case between the parent compounds. Structural relaxations in supercells show that for different patterns such arrangement is indeed global and not an average of local properties. The lack of local geometry features also corroborates the CPA approach taken. The colors distinguish the chemical species: pink, blue, orange, and gray stand for Mn, Si, Fe, and Ni, respectively.

$Mn_{0.5}Fe_{0.5}NiSi$ (using as reference the structure determined for the $Mn_{0.5}Fe_{0.5}NiSi_{0.95}Al_{0.05}$ sample): one where there are two well-separated phases MnNiSi and FeNiSi; one where the occupation is mixed but ordered; one with random disorder (generated within the SQS method [56]). The calculations were performed with the PBE exchange-correlation functional (GGA) [57], which generally performs well in the prediction of structural properties. Moreover, the standard PAW potentials provided by the code [58] and a kinetic energy cutoff of 675 eV were considered. As convergence criteria for the structural relaxation, it was taken that the norms of all the forces should be smaller than 0.001 eV/Å.

The Ni-Si framework relaxes homogeneously for all considered patterns, i.e., without forming localized features as can be seen in Fig. 7. These results support that the structure

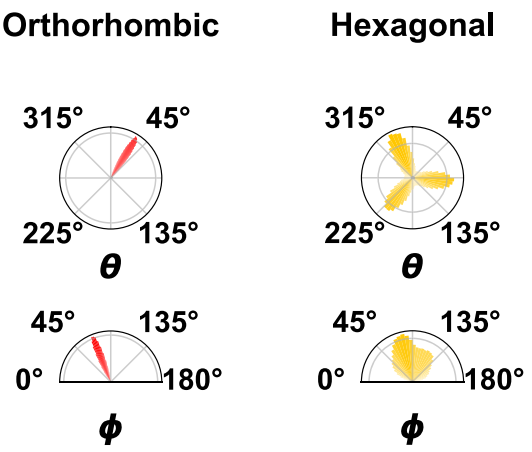

FIG. 8. Statistical distribution of the spin orientations (spherical coordinates with polar angle θ and azimuthal angle ϕ, in the x-y plane) relaxed in the magnetic simulations at $T = 25$ K for the orthorhombic (left) and hexagonal (right) phases.

refined from the XRPD pattern is not an average of local features but an actual representation of the crystalline structure. The lack of local geometry features also validates the use of the CPA to describe the chemical disorder in first-principles calculations.

APPENDIX C: SPIN DISTRIBUTION

Figure 8 presents the statistical distribution of the relaxed spin orientations in the Monte Carlo simulations. In the case of the orthorhombic phase, the spins are oriented along a well-defined direction, more exactly along the z direction since $\theta \approx 0^\circ$. Such a distribution corresponds to the expected ferromagnetic configuration. $\theta \approx 90^\circ$ corresponds to the case where the spins align in the x-y plane. In the case of the hexagonal phase, one can distinguish three evenly spaced directions of the spin orientation in the x-y plane. This threefold symmetry may correspond to a frustrated spin configuration arising from competing ferromagnetic and antiferromagnetic couplings, but further calculations are necessary to confirm such a hypothesis. With the data available, it is only possible to conclude that the hexagonal phase exhibits a noncollinear spin configuration with a finite magnetization due to the asymmetry in the spin distribution along the z direction.

APPENDIX D: EFFECT OF IMPURITY PHASE

An $MgZn_2$-type hexagonal impurity phase has been observed for all studied compounds as seen in Fig. 9(a) for the XRPD refinement of the $x = 0.5$ compound. A likely similar (reported as unknown) impurity phase was observed by Biswas *et al.* [9]. From the SEM and EDS analysis, the chemical compositions of different surface regions [denoted as 1, 2, and 3 in Fig. 9(b)] for the $x = 0.5$ compound have been determined. Regions 1 and 2 have a chemical composition of $Mn_{0.46}Fe_{0.55}Ni_{1.1}Si_{0.85}Al_{0.05}$ and $Mn_{0.46}Fe_{0.49}Ni_{1.16}Si_{0.85}Al_{0.05}$, respectively, which is as expected within the error limit of the EDX analysis. However, region 3 exhibits a Fe-deficient chemical

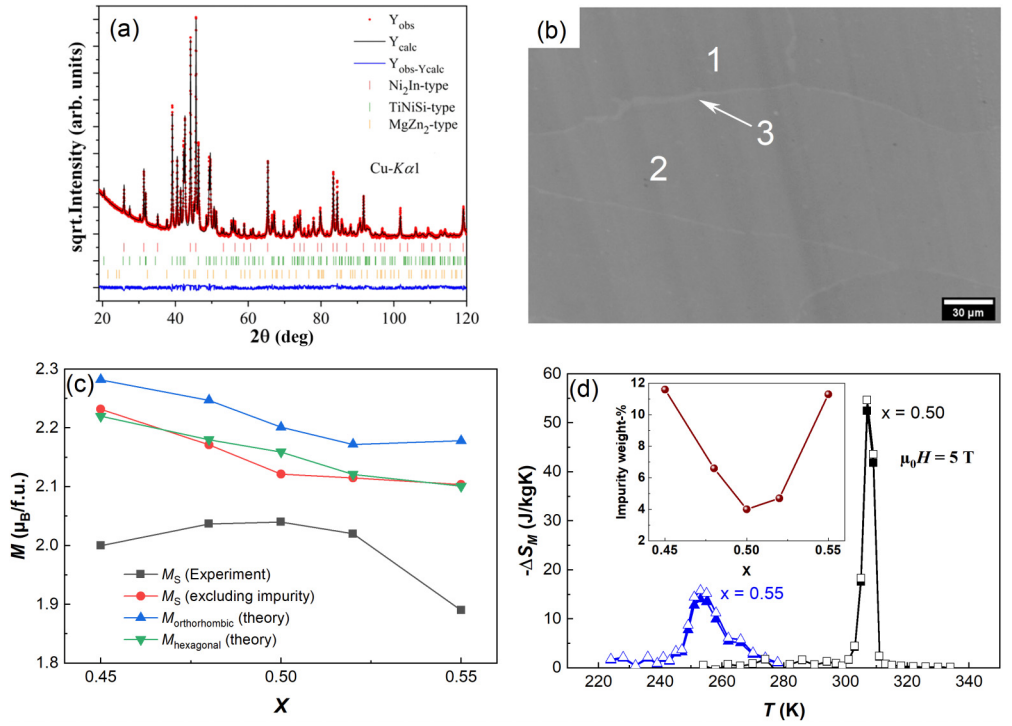

FIG. 9. (a) XRPD refinement for the $x = 0.5$ compound. The data was collected at ambient conditions. (b) SEM/EDS analysis of the $x = 0.5$ compound; the white regions correspond to the impurity phase, which has the chemical composition $Mn_{0.9}Fe_{0.1}Ni_{1.2}Si_{0.7}Al_{0.04}$. (c) Calculated magnetic moment per formula unit and the measured saturation magnetization of the studied compounds. (d) Isothermal entropy change with (solid symbols) and without (hollow symbols) considering the impurity phase. Inset shows the wt. % of the impurity phase.

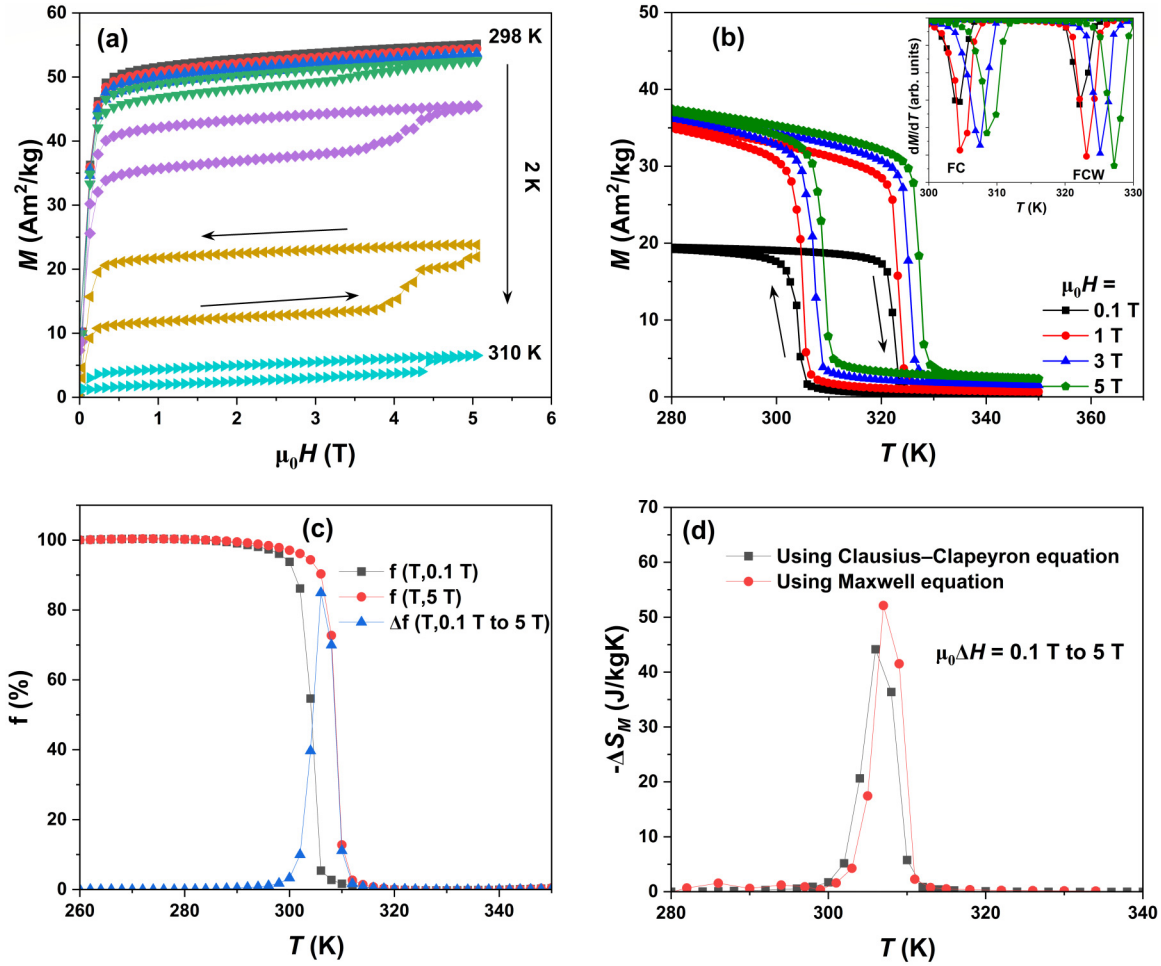

FIG. 10. Magnetization results for the $x = 0.5$ compound. (a) Isothermal magnetization curves recorded following the phase reset cooling cycle protocol. (b) Temperature-dependent magnetization for different applied magnetic fields; the inset shows the derivative of the magnetization with respect to temperature. (c) Temperature-dependent variation of the normalized magnetization at the magnetic fields 0.1 T and 5 T and their difference using Eqs. (7) and (8), respectively. (d) Isothermal entropy change using Maxwell's and Clausius-Clapeyron's relations for a magnetic field change from 0.1 T to 5 T.

composition, $Mn_{0.9}Fe_{0.1}Ni_{1.2}Si_{0.7}Al_{0.04}$, and can possibly correspond to the $MgZn_2$-type hexagonal impurity phase observed in XRPD.

The wt. % of the impurity phase increases if the Fe/Mn ratio deviates from unity, as is seen in the inset of Fig. 9(d). However, from magnetization measurements, no extra magnetic phase transition has been observed below 400 K. The existence of a nonmagnetic impurity phase will introduce a systematic error when determining the magnetization of the compound. In Fig. 9(c), the measured values of the saturation magnetization (M_S) at 10 K for the studied compounds are shown, which do not match with the theoretically calculated trend for the total magnetization. However, if the mass of the impurity phase is subtracted from the mass of the samples before calculating the magnetization of the compounds, the experimental values of $M_S(x)$ are in agreement with the theoretical results. Similar mass corrections have been performed for the calculation of ΔS_M and the results are shown in Fig. 9(d). It can be concluded that the effect of this impurity phase is negligible for the calculated values of ΔS_M.

APPENDIX E: USE OF CLAUSIUS-CLAPEYRON EQUATION

In this work, the isothermal entropy change ($-\Delta S_M$) has been calculated using Maxwell's relation. In this method, isothermal magnetization curves are recorded [as shown in Fig. 10(a)] and then, using Eq. (2), the values of $-\Delta S_M$ are calculated. Another possible way of calculating $-\Delta S_M$ is to use Clausius-Clapeyron's (CC) relation [44,45],

$$\Delta S_M \approx -\Delta f \Delta M \frac{dH}{dT_C}, \tag{6}$$

where ΔM is the field-independent magnetization difference between the paramagnetic and ferromagnetic states, $\frac{dH}{dT_C}$ is the inverse of the rate of change of the T_C with applied magnetic field, and $\Delta f(T, \Delta H)$ is the change of normalized magnetization $f(T)$ for a magnetic field change of ΔH. $f(T)$ is defined as

$$f(T) = \frac{M(T) - M_{PM}(T)}{M_{FM}(T) - M_{PM}(T)}, \tag{7}$$

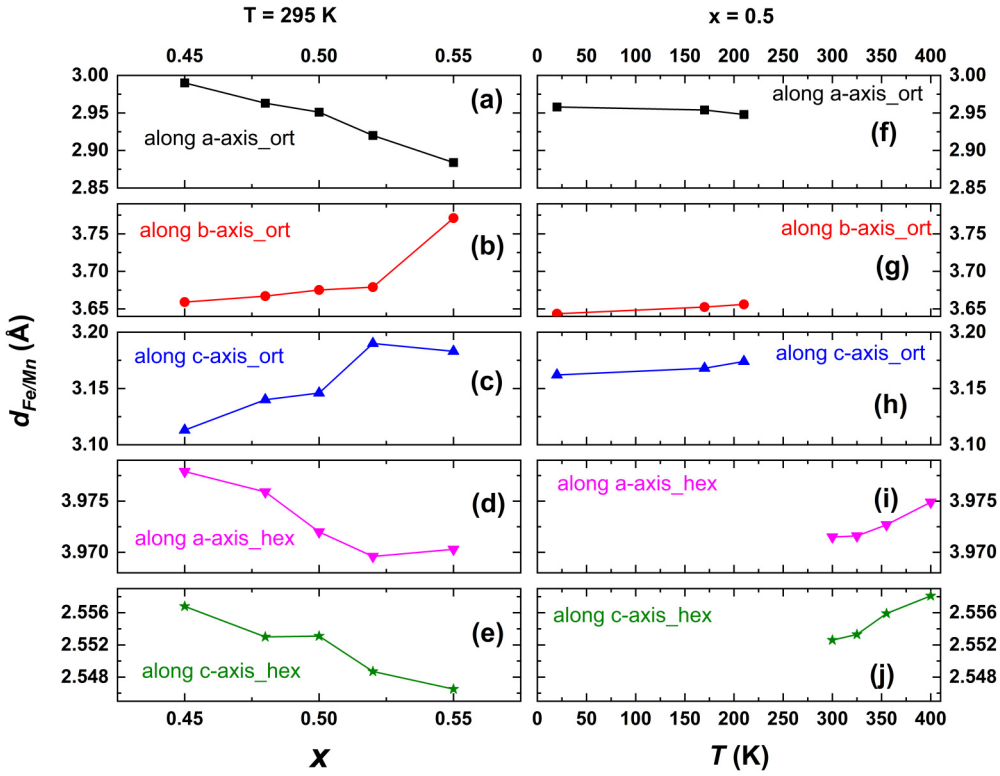

FIG. 11. [(a)–(e)] Fe concentration (x) dependent variation of Fe/Mn atomic distance ($d_{\mathrm{Fe/Mn}}$), along different crystallographic directions of the orthorhombic (ort) and the hexagonal (hex) phase at 295 K. [(f)–(j)] Temperature-dependent variation of $d_{\mathrm{Fe/Mn}}$ for the $x = 0.5$ compound along different directions of the two phases; the data are only shown for the major phase, i.e., the hexagonal phase in the paramagnetic region and the orthorhombic phase in the ferromagnetic region.

where $M_{FM}(T)$ and $M_{PM}(T)$ correspond to the magnetization values for the ferromagnetic and paramagnetic states, respectively. Δf is then calculated as the difference between $f(T)$ corresponding to the fields H_{final} and H_{initial},

$$\Delta f(T, \Delta H) = f(T, H_{\mathrm{final}}) - f(T, H_{\mathrm{initial}}). \tag{8}$$

Temperature-dependent magnetization curves at different applied magnetic fields are shown in Fig. 10(b) for the $x = 0.5$ compound. Using these results, $f(T)$ at 0.1 T and 5 T was calculated, along with the difference (Δf); the results are shown in Fig. 10(c). The detailed calculation steps follow the work of Xu *et al.* [45]. For the $x = 0.5$ compound, the value of ΔM is $\sim$52 Am^2/kg and $\frac{dT_C}{dH}$ is $\sim$1 K/T [see inset of Fig. 10(b)]. Using these values in Eq. (6) resulted in the temperature-dependent $-\Delta S_M$ values shown in Fig. 10(d). For comparison, $-\Delta S_M(T)$ calculated using Maxwell's relation for a magnetic field change from 0.1 T to 5 T are also included in Fig. 10(d). The results show good agreement, even though the calculated $-\Delta S_M(T)$ values using the CC method are slightly lower. This might be traced back to the basic assumptions made in the CC method that the temperature-dependent magnetization is a step function at T_C with a 100% phase change [59] and that ΔM is not a function of the applied field [60]. Moreover, the CC method assumes that the volume of the sample remains constant at the transition, which is not true for a magnetostructural transition where the transition is also associated with a volume change. In addition, there is a temperature shift between the two methods, which is due to different cooling protocols; for the CC method the sample is continuously cooled, while for the method using Maxwell's relation, the sample is heated to its paramagnetic state before cooling to the desired temperature, i.e., the phase reset cooling protocol. For a first-order magnetic phase transition, similar temperature shifts have previously been observed in adiabatic temperature measurements comparing continuous and phase reset cooling [61] results.

APPENDIX F: Fe/Mn ATOMIC DISTANCE AND MAGNETIC INTERACTION

In any magnetic system, the magnetic transition temperature (T_C) is highly influenced by the interatomic magnetic interaction. This magnetic interaction depends upon the interatomic distances between two magnetic atoms. Similarly, in the (Mn,Fe)NiSi system, the magnetic interaction and its corresponding T_C should be related to the interatomic distances between Fe/Mn atoms ($d_{\mathrm{Fe/Mn}}$). However, as discussed in Sec. III B, there are orthorhombic and hexagonal phases throughout the magnetic phase transition region; the $d_{\mathrm{Fe/Mn}}$ is not unique. In the orthorhombic phase, there are three (along the a, b, and c axis) and, in the hexagonal phase, two (along the a and b axis) values for $d_{\mathrm{Fe/Mn}}$ are observed from the XRPD analysis.

In Figs. 11(a)–11(e) all these distances are shown for the variation of x at 295 K temperature. In Figs. 11(f)–11(j) the temperature-dependent variation of $d_{\mathrm{Fe/Mn}}$ for the $x = 0.5$ compound is shown. At temperatures

TABLE III. Variation of calculated magnetic properties of $Mn_{0.5}Fe_{0.5}NiSi_{0.95}Al_{0.05}$ with the geometrical parameters on the TiNiSi-type representation. The magnetic ordering temperature T_C was calculated using the mean-field approximation. The experimental structures are highlighted in bold.

Wyckoff positions	c (Å)	a/c, b/c	Volume (Å^3)	Mag. mom. (μ_B/cell)	T_C (K)
hex phase	**6.88**	**0.74, 0.58**	**139.53**	**8.63**	**305**
ort phase	6.88	0.74, 0.58	139.83	8.32	611
ort phase	6.94	0.74, 0.58	143.54	8.58	617
ort phase	**6.94**	**0.81, 0.53**	**142.79**	**8.80**	**823**

where only small amounts of phases are present (below 20 wt. %), the refinement process does not converge properly when refining structural parameters (x, y, z) for the orthorhombic phase. Conversely, refining only the lattice parameters (a, b, c) does not provide a clear understanding of changes in bond distances, especially for the orthorhombic phase. Therefore, in Figs. 11(f)–11(j) the data for only the major phases (above 80 wt. %) are shown. For a better comparison, the data along each direction of a particular phase are plotted on the same scale. The $d_{Fe/Mn}$ is inversely proportional to the x values along all directions in the hexagonal phase and along the a-axis direction of the orthorhombic phase. Interestingly, $d_{Fe/Mn}$ is proportional to x along the b and c axis of the orthorhombic phase. In comparison with x dependency, the temperature-dependent variation is much smaller (in absolute value) in the orthorhombic phase and comparable in the hexagonal phase. In the hexagonal phase, with the variation of x, $d_{Fe/Mn}$ decreases, and, with the variation of temperature (T), $d_{Fe/Mn}$ increases. On the contrary, in the orthorhombic phase both x, and T, influence the $d_{Fe/Mn}$, with the same decreasing (along a axis) or increasing (along the b and c axis) trend. Hence $d_{Fe/Mn}$ is a function of both x and T. In addition, the phase composition consistently varies with temperature, making it difficult to conclude about the magnetic interaction from the change of atomic distances.

From the J_{ij} calculation [see Fig. 1(c)], it is observed that, if the $d_{Fe/Mn}$ (irrespective of hexagonal and orthorhombic phase) is below 4 Å, the magnetic interaction will be ferromagnetic for the first and second nearest neighbors. In Fig. 11, all distances are below 4 Å, indicating only ferromagnetic interaction for the first nearest neighbor interaction in the studied compounds.

Comparing the mean-field T_C calculated from the J_{ij} computed for the $x = 0.5$ compound with varying lattice parameters allows us to complement the impact of the $d_{Fe/Mn}$ variation on the magnetic properties. In Table III, two intermediate geometries were examined against the experimental structures in the TiNiSi-type representation: an orthorhombic structure with lattice ratios equal to those in the hexagonal cell (with the c parameter fixed) and an orthorhombic structure with lattice parameters identical to those in the hexagonal cell. One observes a drastic alteration of the estimated T_C with the alteration of the lattice parameter ratios, which partly explains the alteration of the magnetic properties between the orthorhombic phases and hexagonal phases. As evidenced by the result from the other intermediate structure, this accentuated alteration is not caused by the overall variation of the distances between atoms, but by the distortion of the local environment of Mn/Fe sites caused by the lattice parameters' ratio changes. This conclusion is in line with the other major contribution for the sharp distinction of the magnetic properties between phases—the displacement from the high-symmetry Wyckoff positions on the orthorhombic phase [see Fig. 6(a)], which alters the local environments besides altering the $d_{Fe/Mn}$.

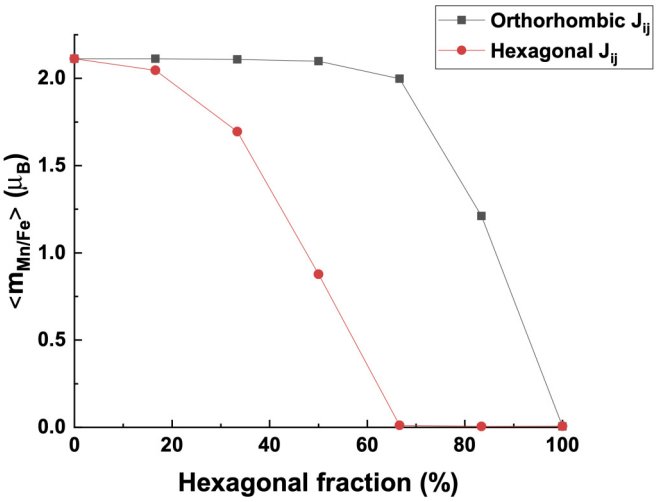

FIG. 12. Calculated average magnetization for the multiphase mixture phase at $T = 25$ K as a function of the hexagonal weight fraction. The data sets refer to two possible cases for the unknown interface exchange parameter J_{ij}^{inter} between phases.

APPENDIX G: ORTHORHOMBIC-HEXAGONAL MIXING

In the simulations for the magnetic multiphase mixture, seven different concentrations of hexagonal phase were considered: 0, 16.7, 33.3, 50, 66.7, 83.3, and 100%. As discussed in the main text, depending on the chosen set of J_{ij}^{inter}, which describes the magnetic interaction between atoms of the orthorhombic and hexagonal phases, the magnetic order is affected differently by the hexagonal fraction. In Fig. 12, we observe for the $J_{ij}^{inter} = J_{ij}^{ort}$ scenario that with increasing hexagonal fraction the magnetization remains constant until 66.7%, while in the other extreme, $J_{ij}^{inter} = J_{ij}^{hex}$, the magnetization drops rapidly with increasing hexagonal fraction. These results align with the spin arrangements simulated for the pure phases—ferromagnetic for the orthorhombic phase and noncollinear for the hexagonal phase; see Fig. 8. In the $J_{ij}^{inter} = J_{ij}^{hex}$ case, the number of AFM couplings in the multiphase mixture grows faster with hexagonal fraction than for the $J_{ij}^{inter} = J_{ij}^{ort}$ case, since such couplings are included not only through the interaction between hexagonal sites (J_{ij}^{hex}) but also between hexagonal and orthorhombic sites (J_{ij}^{inter}). The increased competition between AFM and FM couplings results in noncollinear configurations, with lower magnetization, in order to minimize the energy according to the

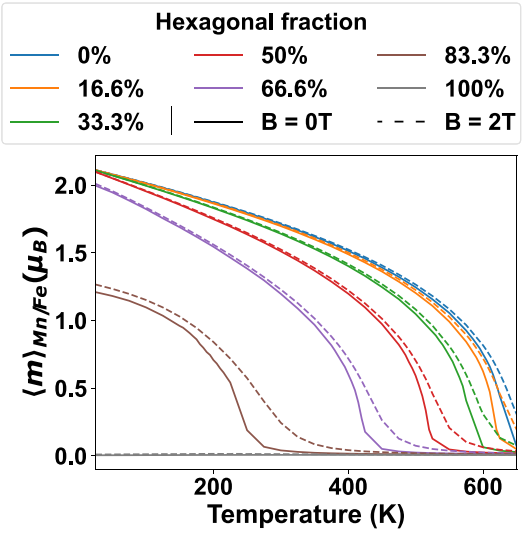

FIG. 13. Temperature-dependent magnetization curves from MC simulations with (dashed lines) and without external magnetic field (solid lines). The colors distinguish different magnetic multiphase mixtures with distinct hexagonal weight fractions.

Heisenberg Hamiltonian [Eq. (1)]. Note that from heat capacity calculations long-range magnetic ordering is observed for all multiphase mixtures, despite no magnetization being observed. The calculated temperature-dependent magnetization for the different hexagonal fractions allows mapping a magnetization surface $M(T, y)$ [see Fig. 5(a) in the main text] being a function of temperature T and the hexagonal fraction y. Applying a bilinear interpolation on $M(T, y)$ and combining with the hexagonal weights from the XRPD refinements (see Fig. 2 in the main text), renormalized to exclude the impurity phase, we can include the temperature-dependent growth of the hexagonal phase in the simulation of the magnetization. The resultant temperature-dependent magnetization using $J_{ij}^{\text{inter}} = J_{ij}^{\text{ort}}$, shown in Fig. 5(b) of the main text, drops in agreement with the experimental result close to T_{st}, capturing better the behavior below T_C. Note that the experimental magnetization curve is stiffer at low temperatures than any of the calculated curves, as this is a known consequence of a classical description of the spins in the simulations.

Given the better performance of the $J_{ij}^{\text{inter}} = J_{ij}^{\text{ort}}$ set, only this case was considered to study the magnetic field response. In Fig. 13 the temperature-dependent magnetization curves can be seen for the different multiphase mixtures, with and without a magnetic field of 2 T. In general, for a given temperature, the change in magnetic response for a multiphase mixture material exposed to a comparably large magnetic field is much smaller than the variation of magnetic response due to a change in material composition. Such behavior is particularly evident at low temperatures but extends up to temperatures where the magnetic transition occurs. A consequence of this is that the magnetic field alone will not modify or change the magnetic ordering, since this is ruled by the temperature-dependent growth of the hexagonal phase close to the structural transition. However, the magnetic field should stabilize the high magnetization phase (the orthorhombic phase) and then change how the phases in the magnetic multiphase mixture evolve with temperature. Thus the magnetic field can indirectly affect the magnetic order and give rise to the measured GMCE.

[1] O. Gutfleisch, M. A. Willard, E. Brück, C. H. Chen, S. Sankar, and J. P. Liu, Magnetic materials and devices for the 21st century: Stronger, lighter, and more energy efficient, Adv. Mater. **23**, 821 (2011).

[2] N. A. Zarkevich and V. I. Zverev, Viable materials with a giant magnetocaloric effect, Crystals **10**, 815 (2020).

[3] J. Liu, Y. Gong, G. Xu, G. Peng, I. A. Shah, and F. Xu, Realization of magnetostructural coupling by modifying structural transitions in MnNiSi-CoNiGe system with a wide curie-temperature window, Sci. Rep. **6**, 23386 (2016).

[4] V. Johnson, Diffusionless orthorhombic to hexagonal transitions in ternary silicides and germanides, Inorg. Chem. **14**, 1117 (1975).

[5] V. Johnson and C. Frederick, Magnetic and crystallographic properties of ternary manganese silicides with ordered Co_2P structure, Phys. Status Solidi A **20**, 331 (1973).

[6] T. Samanta, I. Dubenko, A. Quetz, J. Prestigiacomo, P. W. Adams, S. Stadler, and N. Ali, $Mn_{1-x}Fe_xCoGe$: A strongly correlated metal in the proximity of a noncollinear ferromagnetic state, Appl. Phys. Lett. **103**, 042408 (2013).

[7] C. Zhang, D. Wang, Q. Cao, Z. Han, H. Xuan, and Y. Du, Magnetostructural phase transition and magnetocaloric effect in off-stoichiometric $Mn_{1.9-x}Ni_xGe$ alloys, Appl. Phys. Lett. **93**, 122505 (2008).

[8] E. Liu, W. Wang, L. Feng, W. Zhu, G. Li, J. Chen, H. Zhang, G. Wu, C. Jiang, H. Xu *et al.*, Stable magnetostructural coupling with tunable magnetoresponsive effects in hexagonal ferromagnets, Nat. Commun. **3**, 873 (2012).

[9] A. Biswas, A. K. Pathak, N. A. Zarkevich, X. Liu, Y. Mudryk, V. Balema, D. D. Johnson, and V. K. Pecharsky, Designed materials with the giant magnetocaloric effect near room temperature, Acta Mater. **180**, 341 (2019).

[10] L. Lei, Z. G. Zheng, S. Jin, W. H. Wang, C. F. Li, J. Y. Liu, Z. G. Qiu, and D. C. Zeng, The magnetostructural transition and magnetocaloric properties in $Fe_{0.6}Mn_{0.4}NiSi_{1-x}Al_x$ alloys, J. Appl. Phys. **128**, 013904 (2020).

[11] M. L. Arreguín-Hernández, A. Dzubinska, M. Reiffers, J. L. S. Llamazares, C. F. Sánchez-Valdés, and R. Varga, Magnetostructural transition and magnetocaloric effect in $Mn_{0.5}Fe_{0.5}NiSi_{1-x}Al_x$ melt-spun ribbons (x = 0.055 and 0.060), AIP Adv. **13**, 025336 (2023).

[12] K. Momma and F. Izumi, VESTA: A three-dimensional visualization system for electronic and structural analysis, J. Appl. Crystallogr. **41**, 653 (2008).

[13] J. Korringa, On the calculation of the energy of a Bloch wave in a metal, Physica **13**, 392 (1947).

[14] W. Kohn and N. Rostoker, Solution of the Schrödinger equation in periodic lattices with an application to metallic lithium, Phys. Rev. **94**, 1111 (1954).

[15] H. Ebert, D. Koedderitzsch, and J. Minar, Calculating condensed matter properties using the KKR-Green's function method—recent developments and applications, Rep. Prog. Phys. **74**, 096501 (2011).

[16] P. Soven, Coherent-potential model of substitutional disordered alloys, Phys. Rev. **156**, 809 (1967).

[17] G. M. Stocks, W. M. Temmerman, and B. L. Gyorffy, Complete solution of the Korringa-Kohn-Rostoker coherent-potential-approximation equations: Cu-Ni alloys, Phys. Rev. Lett. **41**, 339 (1978).

[18] J. P. Perdew and Y. Wang, Accurate and simple analytic representation of the electron-gas correlation energy, Phys. Rev. B **45**, 13244 (1992).

[19] A. I. Liechtenstein, M. Katsnelson, V. Antropov, and V. Gubanov, Local spin density functional approach to the theory of exchange interactions in ferromagnetic metals and alloys, J. Magn. Magn. Mater. **67**, 65 (1987).

[20] B. Skubic, J. Hellsvik, L. Nordstrom, and O. Eriksson, A method for atomistic spin dynamics simulations: implementation and examples, J. Phys.: Condens. Matter **20**, 315203 (2008).

[21] O. Eriksson, A. Bergman, L. Bergqvist, and J. Hellsvik, *Atomistic Spin Dynamics, Foundations and Applications* (Oxford University Press, Oxford, 2016).

[22] A. Vaez, The magnetic properties of $Mn_xFe_{1-x}NiSi$ (x = 0, 0.25, 0.5, 0.75, 1) alloys, J. Supercond. Nov. Magn. **26**, 1339 (2013).

[23] N. M. Fortunato, A. Taubel, A. Marmodoro, L. Pfeuffer, I. Ophale, H. Ebert, O. Gutfleisch, and H. Zhang, High-throughput design of magnetocaloric materials for energy applications: MM'X alloys, Adv. Sci. **10**, 2206772 (2023).

[24] A. Biswas, N. Zarkevich, Y. Mudryk, A. K. Pathak, A. Smirnov, V. Balema, D. D. Johnson, and V. Pecharsky, Controlling magnetostructural transition and magnetocaloric effect in multi-component transition-metal-based materials, J. Appl. Phys. **129**, 193901 (2021).

[25] A. Szilva, Y. Kvashnin, E. A. Stepanov, L. Nordström, O. Eriksson, A. I. Lichtenstein, and M. I. Katsnelson, Quantitative theory of magnetic interactions in solids, Rev. Mod. Phys. **95**, 035004 (2023).

[26] K. Binder, D. Heermann, L. Roelofs, A. J. Mallinckrodt, and S. McKay, Monte Carlo simulation in statistical physics, Comput. Phys. **7**, 156 (1993).

[27] C. Zhang, H. Shi, Y. Nie, E. Ye, Z. Han, and D. Wang, Thermal-cycling-dependent magnetostructural transitions in a Ge-free system $Mn_{0.5}Fe_{0.5}Ni(Si, Al)$, Appl. Phys. Lett. **105**, 242403 (2014).

[28] S. Ghosh, P. Sen, and K. Mandal, Magnetostructural transition and large magnetocaloric effect in $(Mn_{0.6}Fe_{0.4})$ $NiSi_{1-x}Al_x$ (x = 0.06–0.08) alloys, J. Magn. Magn. Mater. **500**, 166345 (2020).

[29] R. Duraj, R. Zach, and A. Szytuła, Magnetic phase transitions in $NiMnSinGe_{1-n}$ and $NiMn_{1-t}Ti_tGe$ systems under pressure, J. Magn. Magn. Mater. **73**, 69 (1988).

[30] T. Samanta, D. L. Lepkowski, A. U. Saleheen, A. Shankar, J. Prestigiacomo, I. Dubenko, A. Quetz, I. W. H. Oswald, G. T. McCandless, J. Y. Chan *et al.*, Hydrostatic pressure-induced modifications of structural transitions lead to large enhancements of magnetocaloric effects in MnNiSi-based systems, Phys. Rev. B **91**, 020401(R) (2015).

[31] G. A. Landrum, R. Hoffmann, J. Evers, and H. Boysen, The TiNiSi family of compounds: Structure and bonding, Inorg. Chem. **37**, 5754 (1998).

[32] S. Ghosh, A. Ghosh, P. Sen, and K. Mandal, Giant room-temperature magnetocaloric effect across the magnetostructural transition in $(MnNiSi)_{1-x}(FeCoGa)_x$ alloys, Phys. Rev. Appl. **14**, 014016 (2020).

[33] A. Barcza, Z. Gercsi, K. S. Knight, and K. G. Sandeman, Giant magnetoelastic coupling in a metallic helical metamagnet, Phys. Rev. Lett. **104**, 247202 (2010).

[34] S. Ghorai, J. Cedervall, R. Clulow, S. Huang, T. Ericsson, L. Häggström, V. Shtender, E. K. Delczeg-Czirjak, L. Vitos, O. Eriksson *et al.*, Site-specific atomic substitution in a giant magnetocaloric Fe_2 P-type system, Phys. Rev. B **107**, 104409 (2023).

[35] S. Y. Dan'kov, A. M. Tishin, V. K. Pecharsky, and K. A. Gschneidner, Magnetic phase transitions and the magnetothermal properties of gadolinium, Phys. Rev. B **57**, 3478 (1998).

[36] B. Shen, J. Sun, F. Hu, H. Zhang, and Z. Cheng, Recent progress in exploring magnetocaloric materials, Adv. Mater. **21**, 4545 (2009).

[37] C.-B. Rong and J. P. Liu, Temperature-and magnetic-field-induced phase transitions in Fe-rich FePt alloys, Appl. Phys. Lett. **90**, 222504 (2007).

[38] N. Trung, Z. Ou, T. Gortenmulder, O. Tegus, K. Buschow, and E. Brück, Tunable thermal hysteresis in MnFe(P,Ge) compounds, Appl. Phys. Lett. **94**, 102513 (2009).

[39] D. T. Cam Thanh, E. Brück, N. Trung, J. Klaasse, K. Buschow, Z. Ou, O. Tegus, and L. Caron, Structure, magnetism, and magnetocaloric properties of $MnFeP_{1-x}Si_x$ compounds, J. Appl. Phys. **103**, 07B318 (2008).

[40] R. Skini, S. Ghorai, P. Ström, S. Ivanov, D. Primetzhofer, and P. Svedlindh, Large room temperature relative cooling power in $La_{0.5}Pr_{0.2}Ca_{0.1}Sr_{0.2}Mno_3$, J. Alloys Compd. **827**, 154292 (2020).

[41] S. Ghorai, Direct and indirect magnetocaloric properties of first- and second-order phase transition materials, Ph.D. thesis, Acta Universitatis Upsaliensis, 2022.

[42] S. Ghorai, R. Skini, D. Hedlund, P. Ström, and P. Svedlindh, Field induced crossover in critical behaviour and direct measurement of the magnetocaloric properties of $La_{0.4}Pr_{0.3}Ca_{0.1}Sr_{0.2}MnO_3$, Sci. Rep. **10**, 19485 (2020).

[43] K. A. Gschneidner, V. Pecharsky, and A. Tsokol, Recent developments in magnetocaloric materials, Rep. Prog. Phys. **68**, 1479 (2005).

[44] A. Giguere, M. Foldeaki, B. Ravi Gopal, R. Chahine, T. K. Bose, A. Frydman, and J. A. Barclay, Direct measurement of the "giant" adiabatic temperature change in $Gd_5Si_2Ge_2$, Phys. Rev. Lett. **83**, 2262 (1999).

[45] K. Xu, Z. Li, Y.-L. Zhang, and C. Jing, An indirect approach based on Clausius–Clapeyron equation to determine entropy change for the first-order magnetocaloric materials, Phys. Lett. A **379**, 3149 (2015).

[46] R. Skomski and D. J. Sellmyer, Curie temperature of multiphase nanostructures, J. Appl. Phys. **87**, 4756 (2000).

[47] P. Villars and K. Cenzual, Pearson's crystal data: Crystal structure database for inorganic compounds (on DVD), Release 2023/24, ASM International®, Materials Park, Ohio, USA, https://www.crystalimpact.com/pcd/references.htm.

[48] O. K. Andersen, O. Jepsen, and G. Krier, Lectures on Methods of Electronic Structure Calculation, *Engineering Materials and Processes* (World Scientific, Singapore, 1995).

[49] L. Vitos, I. A. Abrikosov, and B. Johansson, Anisotropic lattice distortions in random alloys from first-principles theory, Phys. Rev. Lett. **87**, 156401 (2001).

[50] L. Vitos, The EMTO method and applications in computational quantum mechanics for materials engineers, *Engineering Materials and Processes* (Springer-Verlag, London, 2007).

[51] B. L. Gyorffy, Coherent-potential approximation for a nonoverlapping-Muffin-Tin-potential model of random substitutional alloys, Phys. Rev. B **5**, 2382 (1972).

[52] P. A. Korzhavyi, A. V. Ruban, I. A. Abrikosov, and H. L. Skriver, Madelung energy for random metallic alloys in the coherent potential approximation, Phys. Rev. B **51**, 5773 (1995).

[53] G. Kresse and J. Hafner, *Ab initio* molecular-dynamics simulation of the liquid-metal–amorphous-semiconductor transition in germanium, Phys. Rev. B **49**, 14251 (1994).

[54] G. Kresse and J. Furthmüller, Efficiency of ab-initio total energy calculations for metals and semiconductors using a plane-wave basis set, Comput. Mater. Sci. **6**, 15 (1996).

[55] G. Kresse and J. Furthmüller, Efficient iterative schemes for *ab initio* total-energy calculations using a plane-wave basis set, Phys. Rev. B **54**, 11169 (1996).

[56] A. Zunger, S.-H. Wei, L. G. Ferreira, and J. E. Bernard, Special quasirandom structures, Phys. Rev. Lett. **65**, 353 (1990).

[57] J. P. Perdew, K. Burke, and M. Ernzerhof, Generalized gradient approximation made simple, Phys. Rev. Lett. **77**, 3865 (1996).

[58] G. Kresse and D. Joubert, From ultrasoft pseudopotentials to the projector augmented-wave method, Phys. Rev. B **59**, 1758 (1999).

[59] J. R. Sun, F. X. Hu, and B. G. Shen, Comment on "direct measurement of the 'giant' adiabatic temperature change in $Gd_5Si_2Ge_2$", Phys. Rev. Lett. **85**, 4191 (2000).

[60] K. A. Gschneidner, V. K. Pecharsky, E. Brück, H. G. M. Duijn, and E. M. Levin, Comment on "direct measurement of the 'giant' adiabatic temperature change in $Gd_5Si_2Ge_2$", Phys. Rev. Lett. **85**, 4190 (2000).

[61] S. Ghorai, D. Hedlund, M. Kapuscinski, and P. Svedlindh, A setup for direct measurement of the adiabatic temperature change in magnetocaloric materials, IEEE Trans. Instrum. Meas. **72**, 1 (2023).